POLITECNICO DI TORINO

Collegio di Ingegneria Chimica e dei Materiali

Master of Science Course
in Materials Engineering

Master of Science Thesis

A Study on Colloidal Interactions between Gold Nanoparticles by using Cryogenic Electron Tomography

Politecnico di Torino

EPFL
École polytechnique fédérale de Lausanne

SuNMIL
Supramolecular Nanomaterials and Interfaces Laboratory

Supervisors
Prof. Marco Sangermano - Politecnico di Torino
Prof. Francesco Stellacci - École Polytechnique Fédérale de Lausanne
Dr. Quy Ong Khac - École Polytechnique Fédérale de Lausanne

Candidate
Carla Malinverni

October 2021

POLITECNICO DI TORINO
Collegio di Ingegneria Chimica e dei Materiali
Corso di Laurea Magistrale in Ingegneria dei Materiali

Riassunto della Tesi di Laurea Magistrale (Sessione: Ottobre 2021)

"A Study on Colloidal Interactions between Gold Nanoparticles by using Cryogenic Electron Tomography"

Candidato: Carla Malinverni

Relatori: Prof. Marco Sangermano - Politecnico di Torino

Prof. Francesco Stellacci, - École Polytechnique Fédérale de Lausanne

Dr. Quy Ong Khac - École Polytechnique Fédérale de Lausanne

1. Introduzione

Nel corso degli ultimi decenni, le nanoparticelle sono state oggetto di molti studi e hanno suscitato grande interesse nella comunità scientifica per le loro eccezionali proprietà dipendenti dalle dimensioni nell'ambito della nanoscala. Con il termine "nanoscala" si fa riferimento al *range* dimensionale compreso tra 1 e 100 nanometri. Le nanoparticelle sono implementate in molte applicazioni significative tra cui i sistemi per il trasporto dei farmaci, i sensori calorimetrici o ancora nel campo della diagnostica clinica e biomedica.
Le nanoparticelle d'oro (AuNPs) vengono spesso utilizzate come modello di riferimento per analizzare il comportamento delle nanoparticelle per quanto riguarda le interazioni tra esse, che possono essere studiate per diverse concentrazioni e in solventi con diversa forza ionica. Le nanoparticelle d'oro sono caratterizzate da una banda di risonanza plasmonica di superficie localizzata nello spettro visibile che produce il caratteristico colore rosso e un forte *scattering* della luce. La variazione della forza ionica provoca l'aggregazione delle nanoparticelle, la banda di risonanza viene modificata e la dispersione cambia colore.
La superficie delle nanoparticelle può essere rivestita da agenti protettivi con proprietà specifiche. La stabilità delle nanoparticelle in una dispersione è influenzata da diversi parametri come ad esempio il pH, la temperatura e la presenza di elettroliti.
È fondamentale avere una buona comprensione della stabilità e della cinetica del processo di aggregazione delle nanoparticelle in relazione alla loro applicabilità. Infatti, il comportamento di auto-assemblaggio indotto dall'aggregazione può modificarne le proprietà. Lo studio della loro stabilità può essere determinato a seguito di una serie di misure strumentali.
L'obiettivo di questo lavoro sperimentale è misurare le interazioni tra nanoparticelle d'oro funzionalizzate tramite la tomografia elettronica criogenica (Cryo-ET) al fine di correlare il comportamento di questi sistemi rispetto a quello previsto dalla teoria Derjaguin-Landau-Verwey-Overbeek (DLVO). Quest'ultima è la teoria più conosciuta ed apprezzata in grado di descrivere la stabilità e le interazioni termodinamiche tra due particelle in una dispersione. I dati ottenuti dal Cryo-ET sono validati dalle misure ottenute con la tecnica di *scattering* dei raggi X a piccoli angoli (SAXS).
La teoria DLVO classica considera solo la repulsione elettrostatica e l'attrazione di van der Waals come unici contributi additivi all'interazione di coppia. Le forze DLVO classiche non sono però in grado da sole di predire il comportamento di aggregazione, per cui è stata

introdotta la teoria DLVO estesa che copre una serie di fenomeni come la repulsione dovuta a fenomeni sterici, ma anche le forze di *bridging*, osmotiche, idrofobiche, magnetiche, con cui si riesce a correlare in modo più completo i dati sperimentali per descrivere le interazioni tra le nanoparticelle (Figura I).

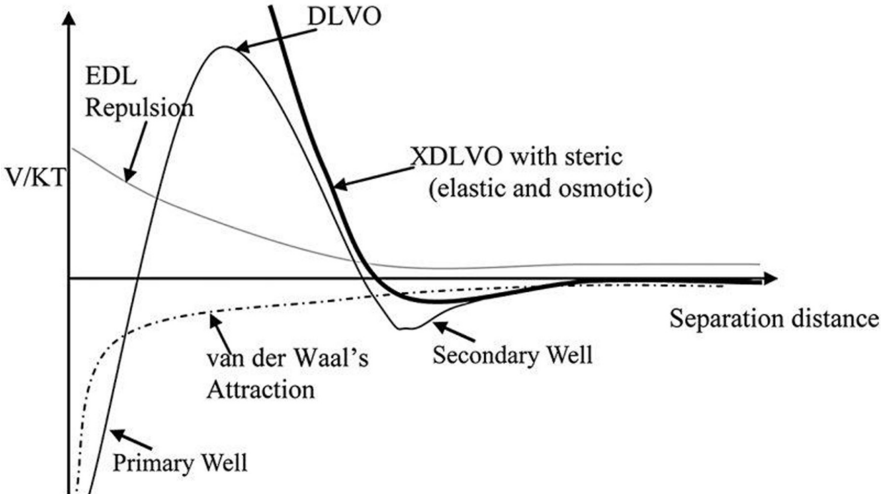

Figura I: Profili dell'energia di interazione per la teoria DLVO classica e estesa in funzione della distanza di separazione tra due particelle [5].

La precisione limitata e l'adeguatezza degli argomenti di *input* nella maggior parte degli approcci teorici di solito limitano una previsione corretta della stabilità delle nanoparticelle cariche in dispersione [4].
In questo lavoro le misure sperimentali sono condotte in funzione di diverse concentrazioni di nanoparticelle in dispersione (5, 10, 20, 40 e 80 mg/mL), per due solventi aventi diversa forza ionica quali l'acqua ultrapura prodotta da *Millipore Corporation* e chiamata Milli-Q e una soluzione 30 mM di cloruro di sodio (NaCl), e infine viene studiato qualitativamente l'effetto della temperatura.

2. Materiali

Per la prima parte del progetto, le nanoparticelle d'oro sintetizzate per indagare gli effetti della concentrazione e della presenza di sale sulle interazioni sono rivestite da *11-mercapto-1-undecane sulfonate* (MUS) usato come ligandi di superficie (Figura II) e hanno una dimensione media di $d_m = 3.0 \pm 0.5$ nm, ottenuta dalle misure con il microscopio elettronico a trasmissione (TEM).

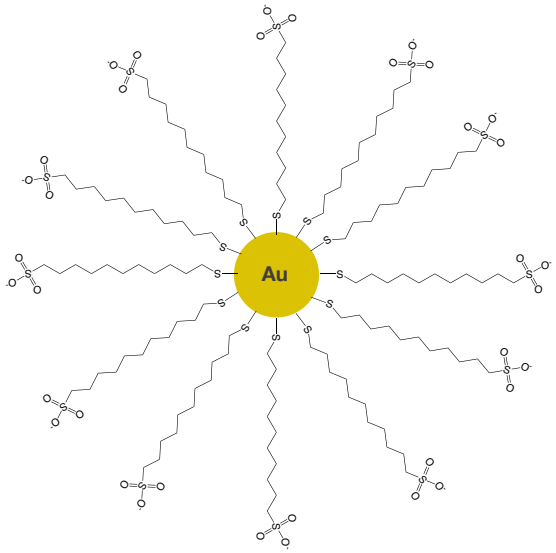

Figura II: Nanoparticella d'oro rivestita da *11-mercapto-1-undecane sulfonate*.

MUS è un ligando tiolato che presenta una lunga catena alchilica idrofoba con acido solfonico come gruppo terminale. Stellacci et al. (2020) hanno studiato il comportamento delle nanoparticelle rivestite di MUS e delle ciclodestrine graffate con MUS come composti antivirali per la loro capacità di inibire alcuni virus, come i virus HSPG-dipendenti, il virus dell'influenza A e anche il virus SARS-CoV-2 [11]. La sintesi di queste nanoparticelle comporta due fasi: la prima consiste nella sintesi di nanoparticelle d'oro rivestite inizialmente con un agente intermedio chiamato oleilammina (OAm). Successivamente, i ligandi di OAm sulla superficie sono sostituiti dai ligandi di MUS in un processo di scambio di ligandi (*ligand-exchange process*). Poiché l'interazione tra oro-azoto è più debole di quella oro-zolfo, la sostituzione dei ligandi di oleilammina con ligandi tiolati è favorita [31]. Grazie alla forte interazione tra il tiolo e la superficie delle nanoparticelle d'oro, questo processo di scambio si è dimostrato essere molto efficace ed è quindi ampiamente utilizzato nella sintesi di nanoparticelle [8].

Per la seconda parte del progetto sullo studio qualitativo riguardante l'effetto della temperatura sull'interazione tra nanoparticelle, vengono usate come riferimento le nanoparticelle d'oro rivestite con poli (N-isopropilacrilammide) (PNIPAM) in quanto le proprietà specifiche del PNIPAM lo rendono uno dei sistemi migliori e più affidabili per testare e stimare questo effetto. Il PNIPAM è un polimero solubile in acqua con gruppi sia idrofobici che idrofili e mostra una transizione reversibile di fase quando viene riscaldato al di sopra di una certa temperatura (per il PNIPAM puro è intorno ai 32°C) in un mezzo acquoso [17]. Questa transizione consiste nel passare da uno stato idrofilo a una temperatura più bassa a uno stato aggregato idrofobico a una temperatura più alta, causando la perdita del 90% circa del suo volume. Questa temperatura è conosciuta come temperatura critica inferiore della soluzione (LCST) o temperatura di transizione di fase del volume (VPTT) [18]. Le sue applicazioni vanno dai sistemi di rilascio di farmaci, microgels, supporto per colture cellulari, *thermal imaging*, sistemi di rilevamento con solubilità variabile e rilascio controllato di biomolecole, come ad esempio le proteine.

3. Metodi

La tomografia elettronica criogenica si basa sulla microscopia elettronica criogenica a trasmissione e permette di osservare i campioni nel loro stato nativo. Nel 2017 è stato assegnato il premio Nobel per la chimica a Jacques Dubochet, Joachim Frank e Richard Henderson per lo sviluppo di questa tecnica. I campioni vengono raffreddati a temperature criogeniche (intorno a -170°C) e incorporati in uno strato di ghiaccio amorfo grazie al raffreddamento molto veloce in etano liquido e successivamente vengono conservati in azoto liquido. L'etano liquido viene usato a causa della sua maggiore capacità termica [21]. La preparazione di un campione per l'analisi tramite Cryo-ET si parte da una griglia di rame su cui è presente un film di carbonio che viene sottoposta a scarica a luminescenza (*glow discharge*) in modo da rendere la griglia idrofilica; in questo modo la dispersione di nanoparticelle si estende sulla griglia. Successivamente la griglia ricoperta viene compressa tra due dischi di carta in uno step chiamato *blotting* per un determinato tempo e con una determinata forza e velocemente immerso in etano liquido e in fine conservato in azoto liquido (Figura III).

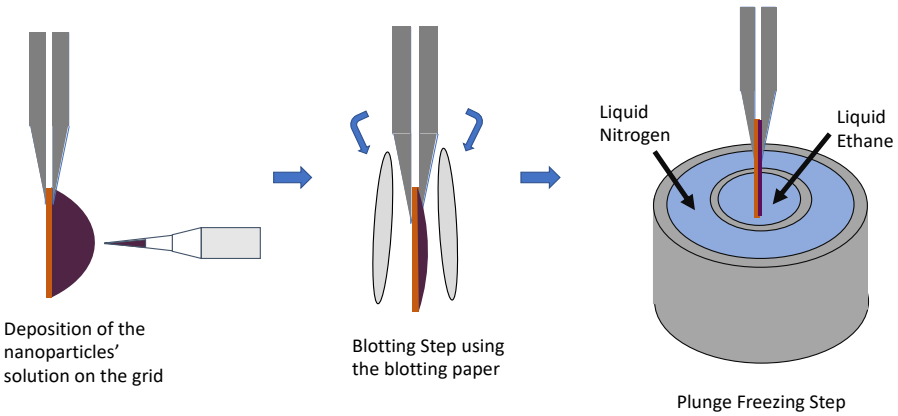

Figura III: Fase di preparazione del campione per l'analisi tramite Cryo-ET.

Dalla misura con il microscopio si acquisiscono attraverso la tomografia molteplici immagini del campione a diverse inclinazioni (da -60° a +60° con un incremento di 2°) chiamate *tilt-series*. Queste immagini vengono poi allineate per produrre la ricostruzione del volume. Le coordinate del centro di gravità delle nanoparticelle sono utilizzate per determinare e calcolare la funzione di distribuzione radiale g(r) attraverso un algoritmo analitico, al fine di valutare quantitativamente le posizioni delle nanoparticelle nelle tre dimensioni e successivamente la curva del potenziale di interazione quindi il potenziale dei sistemi a molti corpi *(many-body potential*) in funzione della distanza di separazione tra le nanoparticelle. La forma della curva può essere influenzata dalla variazione di diversi parametri e condizioni del sistema. Il contrasto dell'immagine dato dalle nanoparticelle d'oro permette di fare la segmentazione dell'immagine tramite soglia d'intensità direttamente alle immagini 3D. La ricostruzione viene eseguita con la tecnica di ricostruzione iterativa simultanea (con 24 iterazioni).

La tecnica di *scattering* di raggi X a piccoli angoli è impiegata in questo nostro lavoro sperimentale per confrontare e convalidare le strutture su scala nanometrica ottenute con metodi ad alta risoluzione come la tomografia elettronica criogenica a trasmissione. Le misure SAXS sono state effettuate dalla Dott.ssa Neda Iranpour Anaraki del centro di analisi Empa dei raggi X di San Gallo, Svizzera, con cui abbiamo collaborato in questo progetto. La misura SAXS consiste nell'esporre un campione contenente la dispersione di nanoparticelle a un fascio primario collimato di raggi X aventi lunghezza d'onda definita (tra 0,05-0,5 nm), a piccoli angoli, circa 0,1 - 5°. Le nanoparticelle producono un'intensità di *scattering* I(q) in funzione del modulo del vettore di *scattering* **q**, che dipende dalla dimensione del fascio:

$$|\mathbf{q}| = (4\pi \sin(\theta)) / \lambda$$

dove 2θ è l'angolo di diffusione tra il fascio primario e quello secondario, λ è la lunghezza d'onda. Il profilo dell'intensità di *scattering* è influenzato dalla distribuzione, dalla dimensione e dalla forma delle nanoparticelle nella dispersione. Per valutare il contributo delle interazioni tra le nanoparticelle rispetto a I(q), vengono analizzate diverse concentrazioni di nanoparticelle nella dispersione [30]. L'intensità di *scattering* I(q) è proporzionale al fattore di struttura S(q) e $|F(q)|^2$, dove F(q) è il fattore di forma che indica la dimensione e la forma delle nanoparticelle. Il fattore di struttura analizza l'interferenza del fascio diffuso e le correlazioni che dipendono dalle interazioni con le nanoparticelle e fornisce una misura delle correlazioni locali del sistema. Il profilo del fattore di struttura è influenzato dalla concentrazione delle nanoparticelle, dall'intensità di *scattering* e dalle loro interazioni [33]. L'applicazione condivisa di queste due tecniche fornisce un approccio molto utile nel favorire un'ampia caratterizzazione delle nanoparticelle d'oro.

4. Discussione dei risultati

Il primo obiettivo del progetto è validare i risultati ricavati dal Cryo-ET rispetto a quelli ricavati dallo *scattering* dei raggi X tramite SAXS per gli stessi campioni alle stesse condizioni.
Il parametro studiato per il confronto è il fattore di struttura S(q). Il fattore di struttura può infatti essere calcolato dalle misure di tomografia crioelettronica a trasmissione attraverso la trasformata di Fourier della funzione di distribuzione radiale g(r) per le diverse concentrazioni. Il massimo presente nelle curve dei S(q) è posizionato ad un valore del vettore di *scattering* pari a $q_{max} \approx 2\ \pi\ /r_{max}$, dove r_{max} corrisponde alla distanza separazione tra le particelle dove si trova il picco di g(r) [40]. I fattori di struttura ottenuti dal Cryo-ET e SAXS sono confrontati in Figura IV.

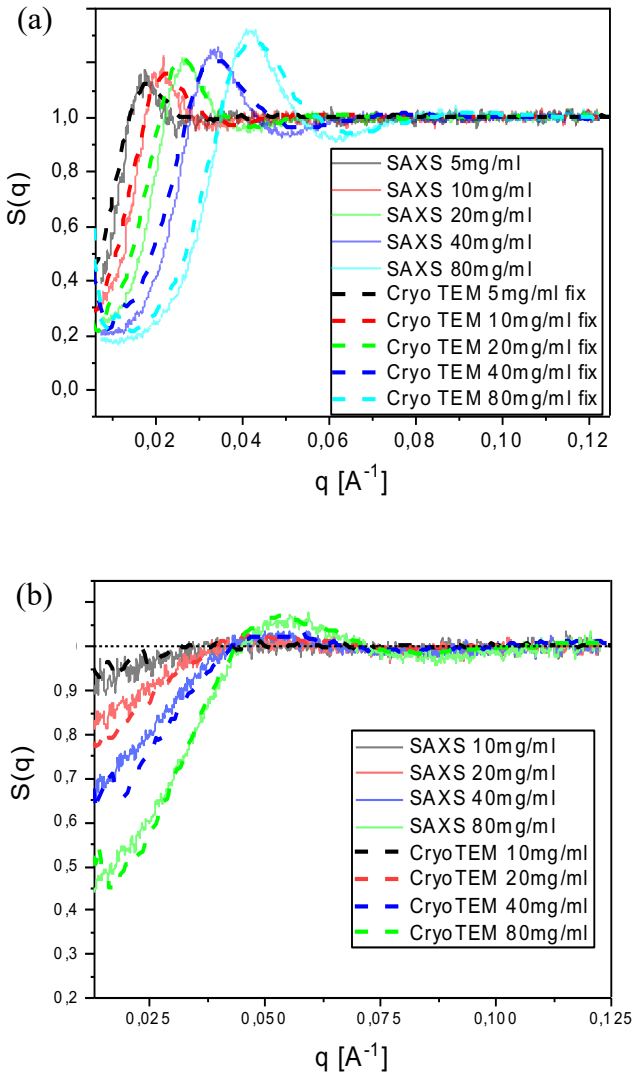

Figura IV: Fattori di struttura S(q) di MUS AuNPs in (a) acqua ultrapura e (b) 30mM NaCl a diverse concentrazioni ottenuti da Cryo-ET (linea tratteggiata) e SAXS (linea completa).

Considerando un piccolo spostamento dovuto alla differenza di concentrazione nel volume del campione per il Cryo-ET nel caso della soluzione in acqua ultrapura, la corrispondenza delle due tecniche dimostra che il processo di congelamento e vetrificazione nell'analisi tramite Cryo-ET non modifica di fatto le proprietà del campione, quindi le nanoparticelle sono caratterizzate nel loro stato nativo.
Successivamente viene valutato il confronto tra il fattore di struttura teorico calcolato usando la teoria DLVO e quello derivato sperimentalmente dalla tomografia elettronica criogenica. Il modello DLVO misura il potenziale di coppia ed è definito per sospensioni colloidali diluite e non considera gli effetti del sistema a molti corpi, mentre i profili ottenuti sperimentalmente dal Cryo-ET sono riferiti alle interazioni a molti corpi.
Quindi, per confrontare i due sistemi, si è utilizzata una soluzione analitica che parte dalla descrizione del sistema nella teoria DLVO come parametri di *input*. I dati teorici vengono poi manipolati utilizzando l'equazione integrale di Ornstein-Zernike (OZ) dalla meccanica statistica che permette la correlazione con i dati sperimentali.
Questa equazione permette di determinare la funzione di correlazione totale h(r) come somma di due contributi, quello diretto, che tiene conto della interazione di coppia tra due particelle 1 e 2, e quello indiretto dovuto alla presenza di tutte le altre particelle presenti nella dispersione.
Questa equazione viene usata per analizzare la funzione di correlazione diretta con quella totale e per convertire i contributi dovuti all'interazione di coppia e quella del sistema a molti corpi. Per risolvere questo calcolo è necessaria una seconda equazione chiamata relazione di chiusura (*closure relation*) dalla quale si può ottenere la funzione di distribuzione radiale e il fattore di struttura che viene poi confrontato con quello misurato sperimentalmente.
Il fattore di struttura teorico è derivato usando un metodo basato sulla soluzione di Ginoza (1982) che utilizza la relazione di chiusura chiamata *rescaled mean spherical approximation* (RMSA) dell'equazione integrale di Ornstein-Zernike, con l'assunzione di un modello di sfere rigide e del potenziale di coppia introdotto da Yukawa [45].
I profili calcolati dalla teoria possono essere adattati manipolando diversi parametri: la frazione volumetrica, che dipende dalla densità numerica delle nanoparticelle, la carica per particella e il parametro di scala $s = \sigma / \sigma'$ il quale sovrastima il diametro del modello a sfere rigide σ introducendo un parametro σ' in modo da mantenere la continuità della funzione di distribuzione radiale $g(r \equiv \sigma') = 0$ per la stessa densità numerica [46].
In Figura V sono riportate le curve dei fattori di struttura ottenuti sperimentalmente e quelli calcolati a partire dalla teoria DLVO.

(a)

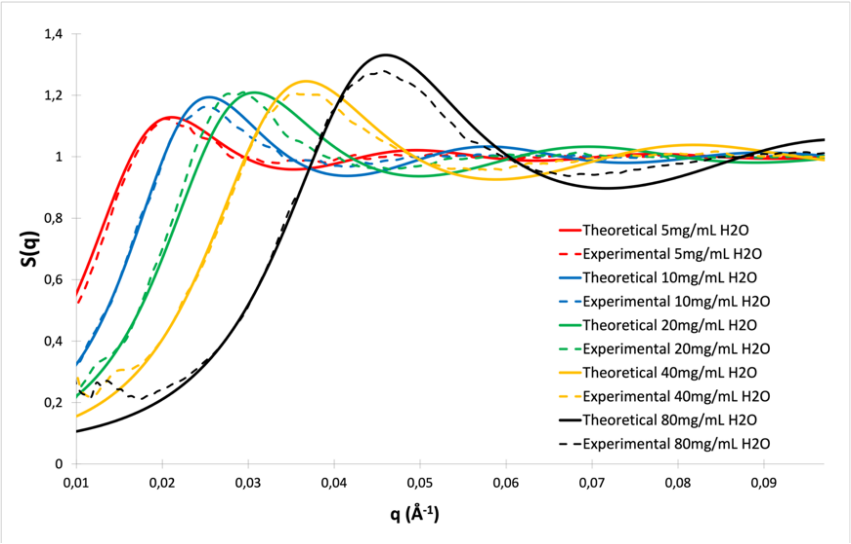

(b)

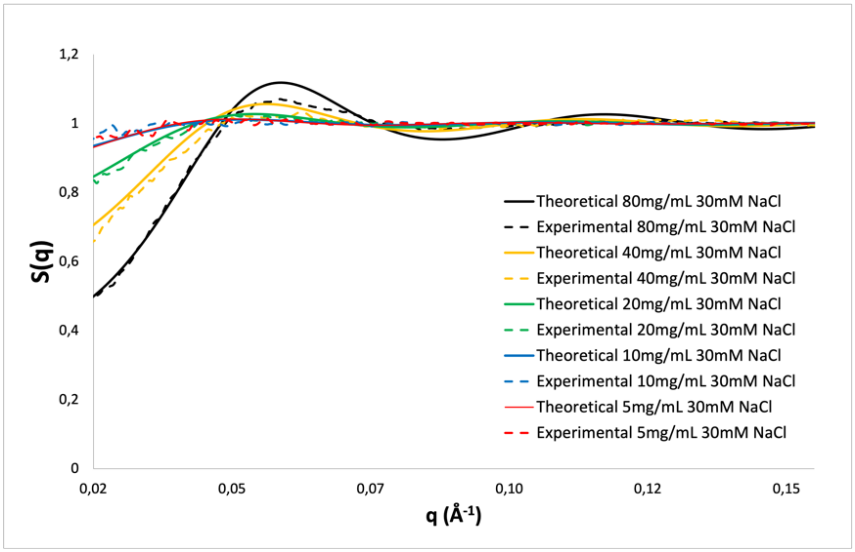

Figura V: Migliore *fitting* dei fattori di struttura teorica S (q) (linea completa) di MUS AuNPs in (a) acqua ultrapura e (b) in soluzione 30mM NaCl a diverse concentrazioni rispetto a quelli sperimentali ottenuti da Cryo-ET (linee tratteggiate).

L'adattamento delle curve calcolate dalla teoria con quelle ottenute nel nostro lavoro viene ottimizzato manipolando il parametro di scala **s** per le diverse concentrazioni così da ottenere un migliore adattamento con i dati sperimentali soprattutto a bassi valori del vettore di *scattering* **q.**
Il problema del *fitting* con la teoria può essere dipendente, ad esempio, dal fatto che, quando le nanoparticelle sono in dispersione, le conformazioni che possono assumere i ligandi dipendono dalle interazioni che essi hanno con il solvente e con le altre nanoparticelle, le quali possono perturbare la loro distribuzione in funzione della loro concentrazione. La complessità di queste conformazioni può causare ulteriori deviazioni dalla teoria [47].

Per osservare invece il comportamento termo-reattivo delle nanoparticelle d'oro PNIPAM sintetizzate. Jones et al. (2016) hanno affermato che l'aggregazione delle nanoparticelle d'oro PNIPAM è fortemente influenzata dal PNIPAM non legato presente come impurità nella dispersione piuttosto che dal PNIPAM che è ancorato sulle nanoparticelle stesse.
Nel caso di soluzioni purificate, il riscaldamento al di sopra della LCST non provoca il cambiamento di colore della dispersione, poiché le catene di PNIPAM collassano ma non causano l'aggregazione delle nanoparticelle [48].
Il fenomeno di aggregazione in una soluzione purificata di nanoparticelle d'oro ricoperte con PNIPAM è indotto dall'aggiunta di sale (in questo caso per le misure è stato usato cloruro di sodio) nella dispersione. Questo abbassa la LCST per cui l'aggregazione delle nanoparticelle si osserva a temperature più basse. Il contributo effettivo del sale nell'aggregazione delle nanoparticelle consiste nella selezione delle cariche sulle nanoparticelle di superficie, per cui la repulsione elettrostatica tra le nanoparticelle d'oro PNIPAM diminuisce.
Grazie all' effetto *salting out*, cioè la disidratazione del PNIPAM che è causata dall'aggiunta del sale, l'interazione idrofoba tra le nanoparticelle aumenta e queste possono agglomerarsi sopra la LCST [49].
Senza la presenza di sali, il cambiamento conformazionale dovuto all'aumento della temperatura sopra la LCST è trattenuto dai legami idrogeno che si generano tra i ligandi di PNIPAM, mentre quando il sale viene aggiunto nel sistema, la riduzione del doppio strato fa diminuire la repulsione elettrostatica dovuta allo *screening* del NaCl, aumentando l'aggregazione. Per alte concentrazioni di NaCl, le crescenti cariche negative delle nanoparticelle d'oro PNIPAM dovute al legame tra i gruppi Cl^{-1} e NH determinano una forte interazione tra i ligandi di PNIPAM ancorati alle nanoparticelle d'oro (Figura VI) [50].

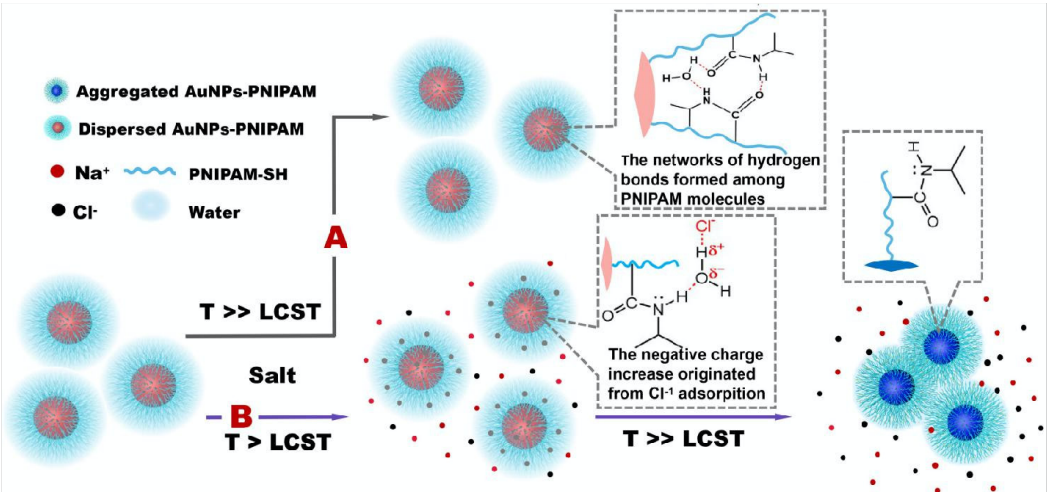

Figura VI: Comportamento termosensibile di PNIPAM AuNPs in diverse condizioni: gli effetti dell'aumento di temperatura sopra il LCST e l'aggiunta di sale [50].

Il comportamento delle nanoparticelle in temperatura e con la presenza aggiuntiva di NaCl viene studiata tramite la microscopia elettronica criogenica a trasmissione (Cryo-TEM). Per confermare che è l'aggregazione delle nanoparticelle è causata solo da una combinazione di

sale e aumento della temperatura, sono acquisite immagini Cryo-TEM di un sistema di nanoparticelle d'oro ricoperte con PNIPAM di 10 mg/mL in 100 mM di NaCl sia a temperatura ambiente (23 ° C) e 100% di umidità relativa, che a temperatura superiore alla LCST (in questo caso sono stati scelti 35°C) a 77% di umidità relativa. A temperatura superiore della LCST si osservano aggregati globulari insieme a nanoparticelle isolate, il che può indicare un meccanismo di aggregazione reversibile di tipo micellare (Figura VII).

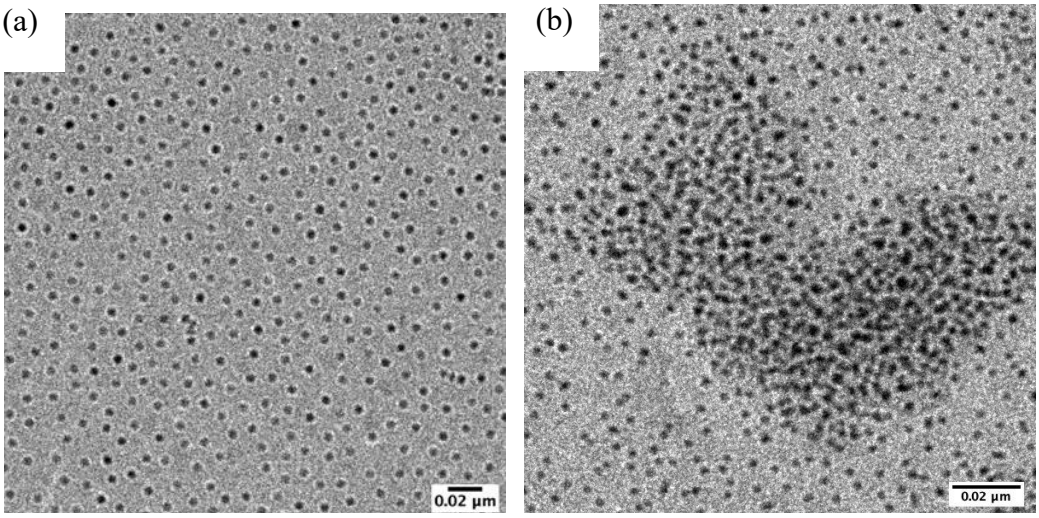

Figura VII: Immagini ottenute con Cryo-TEM di PNIPAM 6kDa AuNPs in 100 mM NaCl (a) a temperatura ambiente e 100% di umidità relativa e (b) a 35 ° C e 77% di umidità relativa.

5. Conclusioni

Le interazioni tra le nanoparticelle d'oro rivestite di MUS sono state studiate in funzione della loro concentrazione, della presenza di sale nella dispersione e dell'effetto della temperatura. Il fattore di struttura calcolato partendo dalla teoria DLVO è stato confrontato con quello derivato sperimentalmente dalla tomografia elettronica criogenica nel caso della dispersione acquosa e di quella contenente 30mM di cloruro di sodio per diverse concentrazioni.

In conclusione, si può affermare che la teoria conferma solo in parte i dati sperimentali, come la dipendenza dalla concentrazione, le interazioni di natura repulsiva, ma non è in grado di descrivere e correlare la stabilità globale delle dispersioni di nanoparticelle.

Al fine di provare metodi diversi con la teoria e testare diverse soluzioni, potranno essere utilizzati altri approcci in futuro. Le prossime sfide potrebbero anche quantificare le interazioni tra nanoparticelle d'oro rivestite con *11-mercapto-1-undecane sulfonate* insieme a *1-octanethiol*, MUS:OT, in cui sono presenti sia un ligando carico (MUS) che un ligando idrofobico (OT), dove l'interazione è più forte.

Le nanoparticelle d'oro rivestite di PNIPAM si sono rivelate un buon modello di riferimento per studiare il comportamento di aggregazione tra le nanoparticelle in funzione dell'aumento della temperatura e della presenza di sale. Le nanoparticelle d'oro PNIPAM possono essere

ulteriormente studiate in futuro attraverso la stima quantitativa delle interazioni tra le nanoparticelle a diverse temperature e mezzi aventi diversa forza ionica e mediante lo studio della concentrazione micellare critica. Il loro comportamento di aggregazione può essere stimato anche grazie all'aiuto della tomografia elettronica criogenica.

Abstract

Over the course of the last decades, nanoparticles have been objects of many researches because of their remarkable properties derived by the dimensions within the nanoscale. The study of their interactions is crucial for their understanding and their implementation in many significant applications such as drug delivery systems, biosensing, clinical and biomedical diagnostics. Cryogenic Electron Tomography (Cryo-ET) is used to evaluate the long-range colloidal interactions of gold nanoparticles within the DLVO (Boris Derjaguin, Lev Landau, Evert Verwey and Theodoor Overbeek) theoretical framework. Cryo-ET is based on the 3D reconstruction of a vitrified nanoparticle dispersion, allowing to derive the 3D radial distribution function of the nanoparticles from which the mean interaction potential and the structure factor can be calculated. The data obtained are validated by small angle X-ray scattering (SAXS) for the same samples prior to the vitrification process. This study is carried out on 11-mercapto-1-undecane sulfonate (MUS)-coated gold nanoparticles as a function of different parameters such as nanoparticle concentration and ionic strength. With known characteristics of the nanoparticles such as purity, core size, surface charge, and ligand density, the DLVO theory is applied to calculate the theoretical structure factors of the nanoparticles under the same experimental conditions, so as to compare them directly with the structure factors experimentally determined. It is concluded that DLVO theory can only partially explain certain aspects of nanoparticle dispersions such as the concentration dependence with some corrections. The effect of temperature on nanoparticle interactions is studied through 2D cryogenic transmission electron microscopy (Cryo-TEM) using gold nanoparticles coated with the thermo-responsive polymer poly(N-isopropylacrylamide) (PNIPAM) as a model. It is shown that the addition of salt lowers the temperature at which the volume phase transition from a hydrophilic state to a hydrophobic aggregated state takes place. At temperatures higher than the phase transition point, Cryo-TEM shows globular aggregate states in presence of isolated nanoparticles, suggesting a micellar-like reversible aggregation mechanism.

Table of contents

1. Introduction and objectives

Over the course of the last decades, nanoparticles have been objects of many studies and have aroused interest in the research community because of their remarkable and exceptional size-dependent properties derived by the dimensions of the nanoscale. The term “nanoscale” refers to the dimensional range between 1 and 100 nanometers.
Nanoparticles have been implemented in many significant applications such as drug delivery systems, biosensing, clinical and biomedical diagnostics, substitutes for genome screenings, calorimetric sensors and their use as suitable analysis detection systems.
Thanks to the large variety of applications, noble metal nanoparticles such as gold nanoparticles (AuNPs) are often used as a reference model to analyze the nanoparticles’ behavior concerning their interactions, that can be studied for different dispersion concentrations and in various media with different ionic strength [1].
Gold nanoparticles are characterized by localized surface plasmon resonance (LSPR) band in the visible spectrum that produces the characteristic red color and a strong scattering of the light. Their spectral behavior can be modified, and they have high surface to volume ratios. The oscillations of the free electrons depend on the size, shape and composition of the nanoparticles. The variation in the ionic strength due to changes of the medium causes the aggregation of the nanoparticles, the LSPR band changes (that corresponds to the shift in the wavelength at which nanoparticles have their maximum absorbance) and the dispersion changes color.
The surface of the nanoparticles can be coated with protective and functionalized agents that have specific properties where for example the repulsion between negative charged agents on the surface can avoid aggregation between the nanoparticles [2].
The stability of nanoparticles is affected by the environmental conditions like pH, temperature and presence of electrolytes, where multiple combinations and contributions are responsible.
A good understanding of the stability and the kinetics of the aggregation process in a gold nanoparticle dispersion is essential in relation to their applicability. In fact, the self-assembly behavior induced by aggregation can modify the nanoparticles’ properties which rely upon their surface chemistry [1].
The study of the interactions between gold nanoparticles in colloidal dispersions is crucial for understanding their behavior in different conditions and for taking advantage of their physical and chemical properties [3].
The control and analysis of their stability can be determined after a series of experimental measurements where the nanoparticle concentration, composition, size can vary.
The restricted precision and adequacy of the input arguments in most theoretical approaches usually limit a correct prediction of the stability of charged nanoparticles in dispersions [4].
The most famous and renowned theory that describes colloidal stability is the Derjaguin-Landau-Verwey-Overbeek (DLVO) theory.
The investigation of the effects of environmental conditions and different concentrations on nanoparticle interactions and distribution can be evaluated and characterized with the help of electron microscopy tomography and scattering methods.

1.1 The DLVO Theory

The DLVO theory takes its name after the initials of the four scientists Boris Derjaguin, Lev Landau, Evert Verwey and Theodoor Overbeek that first developed and studied the stability of aqueous colloidal dispersions. This theory represents the fundament on which the colloidal science and physical chemistry are based, and it is cardinal for understanding the interactions between colloids. It was formulated for the evaluation of interaction potentials between colloids where the size of the particles varies from 1 nm and 1 μm. Since the size of the nanoparticles falls within those studied by the theory, it should be adequate to describe their behavior, but diverse studies proved that it may not be enough to make correlations. The peculiar characteristics of the functionalized gold nanoparticles, like their nanoscale dimensions, their reactivity, the presence of coatings and capping agents challenge the DLVO theory and limit the prediction of their behavior [5].
The DLVO theory describes the short-range interactions that rule the contact between two particles when they can attach or repulse each other, which is indicated by the sticking coefficient α. For example, if α = 1, the probability of binding between two particles at the initial encounter is 100%. The long-range interactions are described by the random motion of Brownian diffusion. The theory started first by describing the case of homoaggregation, when the interaction is between identical particles, followed by heteroaggregation when instead the interaction is between different particles, and subsequently the deposition of a particle on a flat surface that considers the limit case when one particle has larger dimensions than the other [6].
The DLVO theory illustrates the pair interactions between two particles in two main versions: the classical DLVO theory and the extended DLVO theory. The Derjaguin approximation indicates the interaction force among two particles by approximating them to two plates (because of the easier estimation). This force is expressed as

$$F(r) = 2\pi R_{eff} \cdot V(r) \tag{1}$$

where R_{eff} is the effective radius and $V(r)$ is the potential energy per unit area of the two plates as a function on the separation interparticle distance r (it can be also indicated with s). The effective radius can be calculated as a function of the particles' radii R_- and R_+ [6]:

$$R_{eff} = \frac{R_- R_+}{R_- + R_+} \tag{2}$$

The classical DLVO theory states that there are only two types of forces (and thus interaction energies) that describe the pair interaction between particles. It is based on the sum of two contributions that are balanced against each other and determine the assembly of the particles. These two contributions are the electrostatic double-layer repulsion $V_{edl}(r)$ and the van der Waals attraction $V_{vdW}(r)$:

$$V(r) = V_{edl}(r) + V_{vdW}(r) \tag{3}$$

The first one originates from the charged surfaces and the ions present in the solution, while the second one is created by the interactions between the electrons of the particles [5].

The addition of electrolytes in the solution can affect the control of the electrostatic double layer repulsions because of their screening effect on the surface charge of the particles.
The potential energies are often expressed in units of k_BT, where k_B is the Boltzmann constant and T is the temperature, that corresponds to the system's thermal energy.
The classical DLVO theory however oversimplifies the description of the actual contributions and doesn't fully explain the interaction between two particles. These two forces alone don't predict the aggregation behavior, so another more detailed version of the theory has been introduced.
The extended DLVO theory includes several additional contributions to the total interaction force such as steric repulsion forces, but also short-range bridging forces, osmotic, elastic, hydrophobic and magnetic forces. Wijenayaka et al. (2015) proposed a model to better predict and quantitatively describe the stability of gold nanoparticles This model takes into account four forces (Figure 1) that contribute to the total interaction potential [4].

$$\frac{V_{tot}(s)}{k_BT} = \begin{cases} \frac{V_{ele}(s)}{k_BT} = \frac{2\pi\varepsilon_0\varepsilon_r\psi_0^{\,2}a}{k_BT}\ln(1+e^{-\kappa s}) \\ \frac{V_{vdw}(s)}{k_BT} = -\left(\frac{A}{6k_BT}\right)\left(\frac{2a^2}{s(4a+s)} + \frac{2a^2}{(2a+s)^2} + \ln\left(\frac{s(4a+s)}{(2a+s)^2}\right)\right) \\ \frac{V_{osm}(s)}{k_BT} = \frac{4\pi a N_a}{v_1}\phi_p^{\,2}\left(\frac{1}{2}-\chi\right)\left[t^2\left(\frac{s}{2t}-\frac{1}{4}-\ln\left(\frac{s}{t}\right)\right)\right] \\ \frac{V_{ela}(s)}{k_BT} = \left(\frac{2\pi a N_a}{M_W}\phi_p t^2\rho_d\right)\left(\left(\frac{s}{t}\right)\ln\left(\frac{s}{t}\left(\frac{3-\frac{s}{t}}{2}\right)^2\right) - 6\ln\left(\frac{3-\frac{s}{t}}{2}\right) + 3\left(1-\frac{s}{t}\right)\right) \end{cases}$$

Figure 1: Expressions for the different contributions for the total interaction potential proposed by Wijenayaka et al. (2015) [4].

The more information obtained by the addition of these terms better matches experimental data in order to describe the interactions and the level of aggregation among particles.
The classical and the extended DLVO theory are both showed in Figure 2. The primary and secondary wells identify the irreversible and the reversible aggregation between two particles, respectively.

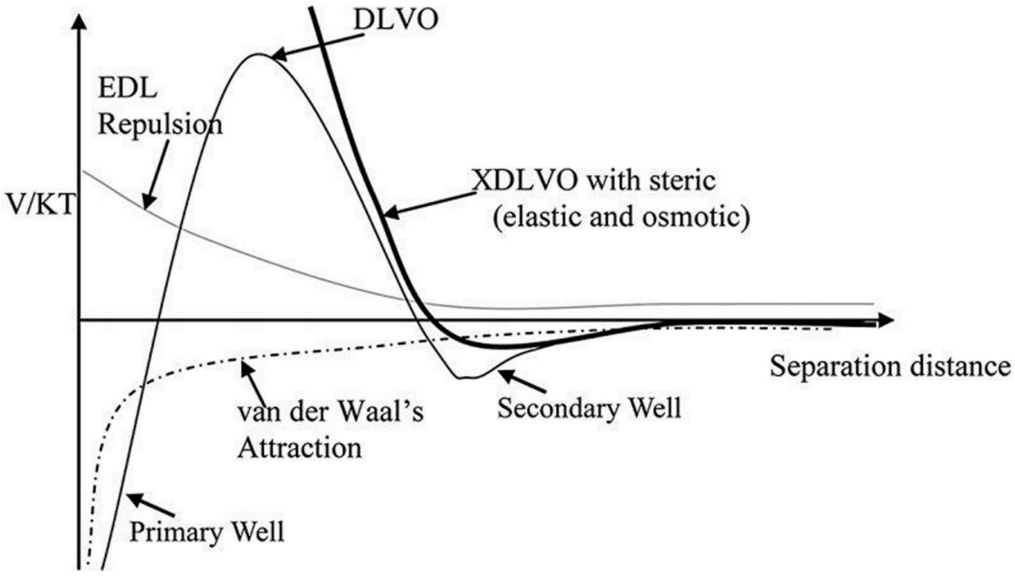

Figure 2: Profiles of the interaction energy as a function of the separation distance between two particles. Both the curves for the classical DLVO theory and the extended DLVO theory are reported, the van der Waals and electric double layer potentials plotted as a function of separation distance between two particles [5].

1.2 Challenges of DLVO Theory in describing the nanoparticle interactions quantitatively

As introduced in the previous section, despite the extension, the DLVO theory's applicability to nanomaterials is not absolute. The challenges focus primarily on several characteristics that describe nanoparticles such as their size, shape, composition, structure and the presence of coatings and capping agents on the nanoparticles' surface.

The Derjaguin approximation can describe well the interaction force among two particles only in the case where the particles' size is bigger than the forces that are involved, which is not the case for small nanoparticles [6].

Gatica et al. (2005) explained that the attraction contribution is usually evaluated among two spherical particles, but the shapes and sizes of the nanoparticles can vary, also because for very small nanoparticles there are more atoms on the surface and the curvature of the surface has to be taken into account. Thus, because of the dimensions at the nanoscale, the electronic structure and the surface reactivity are modified and therefore influence and limit the assumptions made by the theory [7].

Another challenge of the DLVO theory is its inability to predict the aggregation in the secondary well for a given system and salt concentration.

Solvated ions in the solution, due to their size that is often comparable to the small nanoparticles' diameter, are usually considered and counted as point particles which affects the aggregation behavior.

In general, most of the challenges limit the formulation for the quantitative profiles of the interaction potentials of complex systems because of the presence of several indeterminate effects.

1.3 Thesis objectives

The goal of this thesis is to measure the interactions between coated gold nanoparticles in dispersions using cryogenic transmission electron microscopy tomography (Cryo-ET) in order to correlate the behavior of these systems that validates or disproves that predicted by the DLVO theory. The data gained from Cryo-ET are compared with the ones obtained from the same samples from the technique called small angle X-ray scattering (SAXS). The shared application of these two techniques provides a very useful approach that encourages an extensive characterization of coated gold nanoparticles in different conditions.
The experimental measurements are conducted as a function of different parameters, such as the different concentrations of MUS-coated gold nanoparticles in the dispersion for two different media with different ionic strength such as ultrapure water produced using a system manufactured by Millipore Corporation, therefore referred to as Milli-Q water, and a 30mM solution of sodium chloride (NaCl), and finally the qualitative study of the effect of temperature on PNIPAM-coated gold nanoparticles interactions. This project analyzes coated gold nanoparticles that have a mean particle size smaller than 5 nm (the average diameter is around 3 nm).

2. Materials

2.1 Synthesis of MUS-coated Gold Nanoparticles

For the first part of the project, the nanoparticles investigated for the study of the effect of nanoparticle concentration and presence of salt on the interactions consist of gold as inorganic core that is covered with 11-mercapto-1-undecane sulfonate (MUS) as surface ligand, as reported in Figure 3.

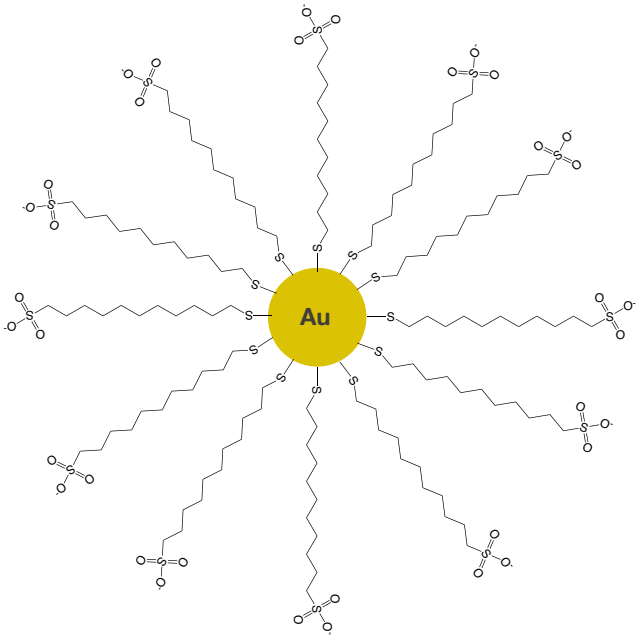

Figure 3: MUS-coated gold nanoparticle.

A ligand is a molecule or ion that donates one or more of its lone pairs of electrons creating a coordination complex with a central metal atom that has a positive charge density. It can range from molecules, organic compounds, polymers, but also proteins, peptides and other biomolecules. It has a very important role since it regulates the colloidal stability, as well as the morphology, functionality, reactivity and size distribution of the nanoparticles and their final properties. The ligands attach on the nanoparticles surface thanks to the presence of anchoring groups that in case of noble metal nanoparticles are usually thiol, amine, carboxyl or phosphine [8]. The molecular formula of MUS is $C_{11}H_{23}O_3S_2^-$ and the molecular weight is around 267.4 g/mol [9] (Figure 4).

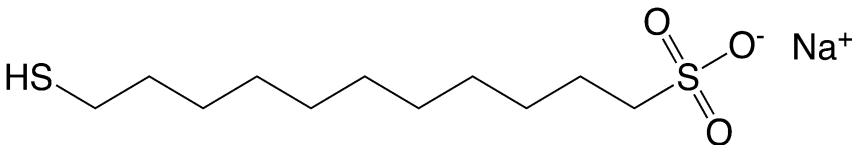

Figure 4: 11-mercapto-1-undecanesulfonate (MUS).

MUS is a thiolated ligand that presents a long hydrophobic alkyl chain with sulfonic acid as terminating group. Its length is estimated to be around 1.7 nm. It has been proved that the presence of the thiol favors the synthesis of smaller nanoparticles from 1 up to 10 nm. It binds strongly to the nanoparticle surface, in particular the bond strength between the thiol and the gold core is around 40-50 kcal mol^{-1} [8].
Their interaction is described through the binding of the deprotonated SH group to the gold surface with the formation of a quasi-covalent bond [10].
MUS-coated gold nanoparticles (MUS-coated AuNPs) are soluble in water and are used in biomedical application, like drug delivery systems and therapeutic agents.
Stellacci et al. (2020) studied the behavior of MUS-coated nanoparticles and MUS-grafted cyclodextrins as antiviral compounds for their ability to inhibit viruses, such as HSPG-dependent viruses, influenza A virus and even SARS-CoV-2 virus [11].
The synthesis of these nanoparticles consists in a two-steps reaction: the first step is the synthesis of gold nanoparticles coated with an intermediate such as Oleylamine (OAm) as an organic ligand. Then the OAm ligands on the gold nanoparticle surface are replaced by the MUS ligands in a ligand-exchange process. Thanks to the strong interaction between the thiol and the gold nanoparticle surface, the thiol-exchange has proved to be very effective and is therefore widely used [8].

2.1.1 Synthesis of Oleylamine-coated Gold Nanoparticles

Oleylamine is a surfactant where the amine group creates a weak interaction with the gold nanoparticle surface.
Its role in the AuNPs synthesis is complex since it acts as intermediate capping reagent, as well as solvent and reducing agent. It is able to reduce gold salt precursors and stabilizes the nanoparticles through electrostatic repulsion, avoiding the formation of aggregates and degradation. It is used as a weakly coordinating ligand that covers the nanoparticle core with a hydrophobic shell and allows it to have high quality, stability and size tunability of the nanoparticles [12].
The core size and the dispersity of the nanoparticles can be modified with varying the reaction temperature, the nanoparticles concentration and the choice of the solvent.
By heating the precursor solution, it has been shown that the average gold nanoparticle size decreases [13].
The molecular formula of OAm is $C_{18}H_{37}N$ and the molecular weight is around 267.5 g/mol [14] (Figure 5).

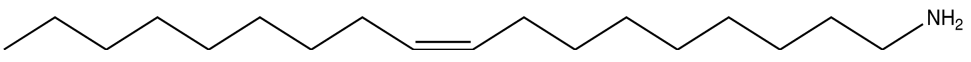

Figure 5: Oleylamine (OAm).

Since the interaction between gold surface and nitrogen is weaker than the gold-sulfur, the exchange and replacement of the oleylamine ligand with a thiol ligand is favored [15].
The hydrophobic OAm-coated AuNPs obtained are dispersed in polar aprotic solvents such as dichloromethane (DCM), but they are not soluble in water.
After the ligand exchange reaction, the nanoparticles with the replaced ligand are transferred and are soluble in polar protic solvents such as water [12].

Chemicals:

- Tetrachloroauric (III) acid trihydrate ($HAuCl_4 \cdot 3H_2O$) (ACS reagent, Acros Organics)
- Oleylamine (approximate C18-content 80-90%, Acros Organics)
- Dichloromethane (DCM, ≥ 99.8%, HPLC grade, Fisher Chemical)
- Tert-Butylamine-Borane Complex (tBAB, 97%, Sigma-Aldrich)
- n-Octane (98%, abcr GmbH)
- Ethanol (analytical reagent grade, ≥ 99.8%, Fisher Chemical)
- Milli-Q Water (resistivity of 18.2 MΩ ·cm at 25°C, total organic carbon < 5ppb)

Experimental Setup:

- Glasswares (Duran)
- Magnetic stir bars
- Magnetic Stirrer (IKA RTC basic)
- Precision Scale (Mettler Toledo)
- Vortex mixer
- Ultrasonic bath Sonicator
- Centrifuge (Sorvall Legend X1R, Thermo Scientific)

The t-butylamine-borane complex is used as an extra reducing agent in order to favor nucleation and facilitate the formation of smaller and monodisperse nanoparticles [13].

Procedure:

588.5 mg of the tetrachloroauric (III) acid trihydrate $HAuCl_4 \cdot 3H_2O$ powder is placed directly into a 500 mL three-necked round bottom flask. A solvent mixture of 48 mL of oleylamine and 60 mL of n-octane is added gently at room temperature. The three necks are closed with rubber septums and the solution is then left stirring to dissolve the solid powder (speed around 900 rpm) forming a yellow solution (Figure 6).

Figure 6: Addition of gold precursor and ligands in the three-necked flask.

When the $HAuCl_4 \cdot 3H_2O$ powder is completely dissolved, the reaction is carried out under the protection of an inert gas such as argon (a flow is added for about 10 minutes). To do that, a needle is placed in the left neck of the flask and a needle with a balloon filled with argon is placed in the right one (Figure 7).

Figure 7: Experimental setup of synthesis of oleylamine-coated nanoparticles with flow of argon to provide water-free conditions.

To prepare the reducing solution, 522.4 mg of t-butylamine-borane complex is dissolved in 12 mL of oleylamine in a separate glass vial. This solution is sonicated and stirred to dissolve the complex. With a disposable syringe of 20 mL, the reducing solution containing the complex

and oleylamine is added through the central neck of the flask in one single shot. After the injection of the solution containing the tert-butylamine-borane complex into the flask, the mixture changes color to dark red-purple due to the fast nucleation and creation of the gold complex with the oleylamine ligands (Figure 8).

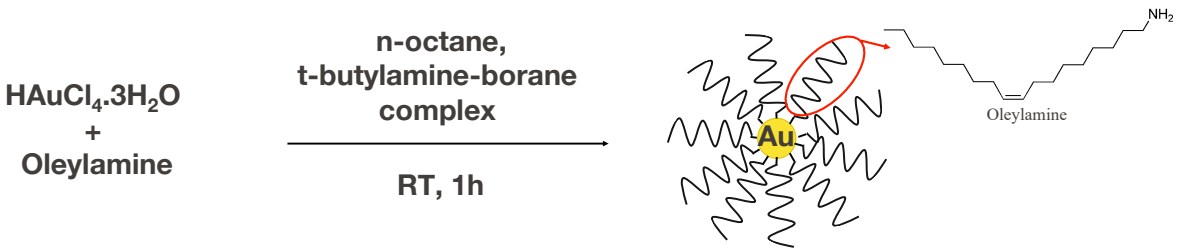

Figure 8: Synthesis of oleylamine-coated gold nanoparticles.

The stirring is decreased around 300 rpm and the system is left reacting in argon atmosphere. After one hour the stirring is stopped, the needle with the balloon and the rubber septums are taken off, and 180 mL of ethanol is added in order to quench the reaction and precipitate the product.
The mixture is transferred in four 50 mL polypropylene falcon tubes. 25 mL of the solution containing the nanoparticles and then 20 mL of ethanol are added to each falcon. The falcons are then centrifuged at 5000 rpm for 5 minutes (Figure 9).

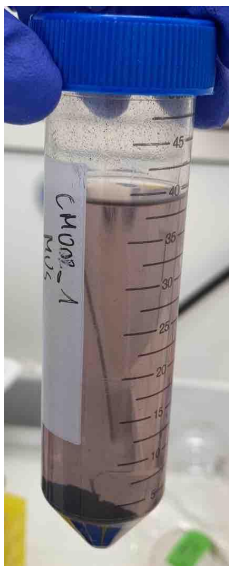

Figure 9: Falcon tube with precipitated and centrifuged oleylamine-coated gold nanoparticles in ethanol.

After centrifugation the supernatant is removed. This step is repeated until all the nanoparticles are transferred into falcons. Then, the nanoparticles in each falcon are re-dispersed in 45 mL of

ethanol and centrifuged again at 5000 rpm for 5minutes. This step is repeated 7 times, in order to wash the nanoparticles and collect the nanoparticle dispersion.
Finally, the OAm-coated AuNPs are finally dissolved in 2 mL of dichloromethane and then the falcon tubes are left overnight in a vacuum dessicator to let the dichloromethane dry. The amount of oleylamine-coated gold nanoparticles obtained is around 250 mg.

2.1.2 Ligand Exchange Reaction

The oleylamine-coated gold nanoparticles undergo a thiol-for-agent ligand exchange reaction. The ligand exchange is a grafting-to approach in which a ligand is replaced by another, in this case a thiol-for-oleylamine. It is one the most accurate methods for controlling the size and the size distribution of the gold nanoparticles [12]. In order to obtain complete and homogeneous exchange of the ligands, the replacing ligands are introduced in large excess, in this case it has been estimated an excess of 20:1. The two-phase ligand exchange reaction is explained in Figure 10.

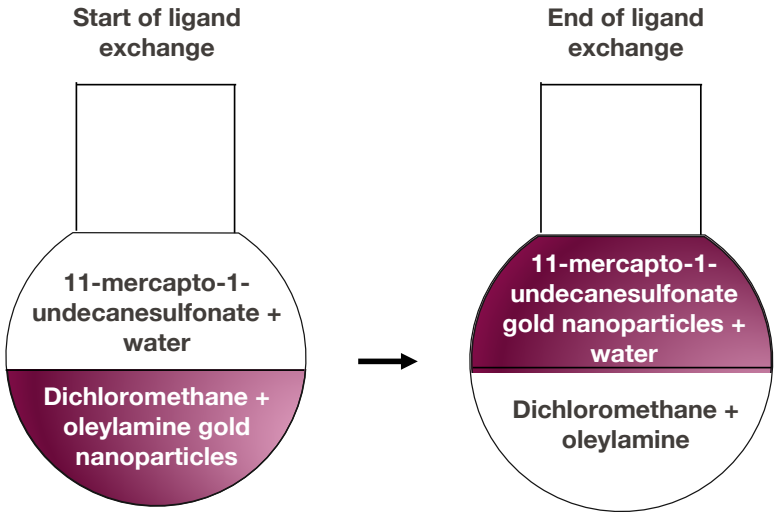

Figure 10: Two-phase ligand exchange (ideal case).

59.8 mg of the oleylamine gold nanoparticles previously obtained are dissolved in 10 mL of DCM. In a separate glass vial are added 214.2 mg of MUS in 20 mL of Milli-Q water. Both powders are dissolved by vigorous mixing and ultrasonication.
The solution containing the oleylamine-coated AuNPs is transferred to a 250mL one-necked round bottom flask, and then 50 mL of dichloromethane is added. Additional 10 mL of DCM is used to rinse the vial and the residual nanoparticles remaining in the vial are transferred to the flask. The MUS solution is added into the flask and then additional 50 mL of Milli-Q water is added. The flask is then closed with a glass cap and let stirring (at around 300 rpm) for 48 hours (Figure 11).

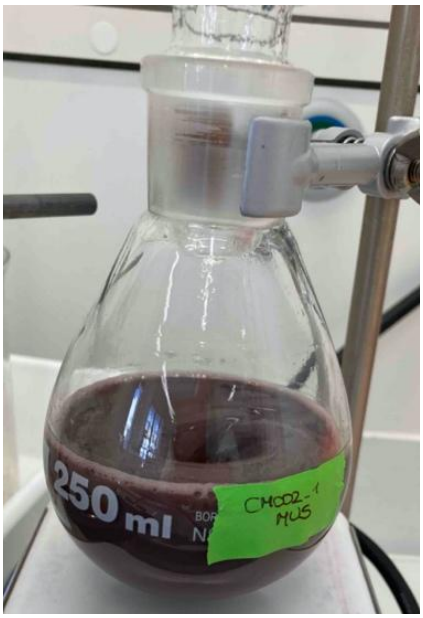

Figure 11: Beginning of the ligand exchange reaction, where the two phases are poured in the 250mL flask.

After two days the stirring is stopped. The water phase containing the MUS-coated gold nanoparticles is transferred into plastic falcon tubes and centrifuged in ethanol for 5 minutes at 3500 rpm, for a total of 5 times. After each centrifugation the supernatant is discarded, new solution and fresh ethanol are added, the precipitates are dispersed again using a vortex mixer and ultrasonic bath. The nanoparticles are then purified with Milli-Q water on Amicon® Ultra-15 centrifugal filter devices (30k molecular weight cut-off) where they are dispersed in water and centrifuged each time for 5 minutes at 5500rpm for another 10 times. As a last step, the nanoparticle solution is transferred to falcon tubes and freeze-dried, obtaining the nanoparticles powder (Figure 12).

Figure 12: Freeze Drying of MUS-coated AuNPs.

2.1.3 ^{1}H-NMR Characterization

In order to verify the effective synthesis and purification of the nanoparticles, nuclear magnetic resonance spectroscopy measurements are conducted, for pure MUS and both for etched and non-etched nanoparticles in deuterated methanol (CD_3OD) and deuterium oxide (D_2O) respectively. The etching solution is iodine (20 mg) dissolved in deuterated methanol (0.4 mL). The etching is obtained by suspending the nanoparticles (5 mg) in the etching mixture (0.6 mL). The ^{1}H-NMR spectra are reported in Figures 13 and 14.

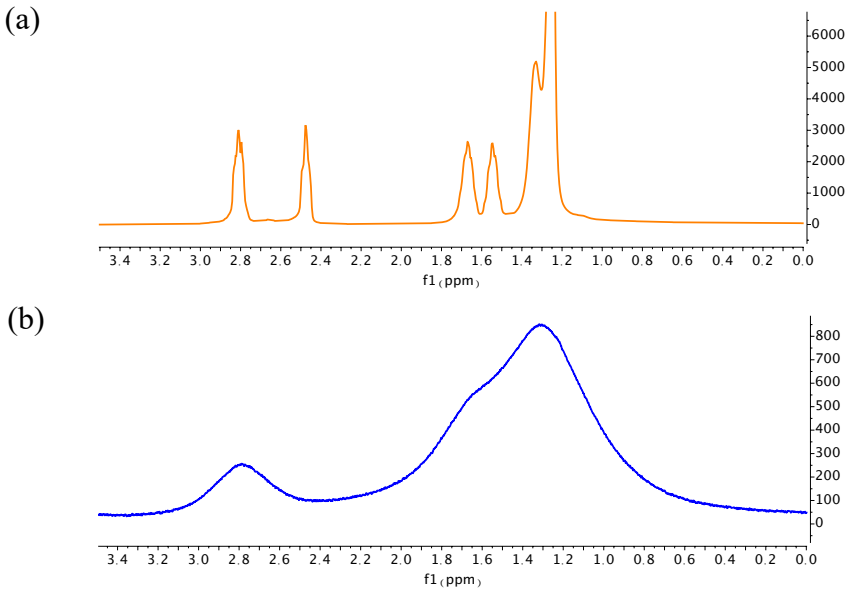

Figure 13: NMR spectra of (a) pure MUS in deuterium oxide and (b) non-etched MUS-coated gold nanoparticles in deuterium oxide.

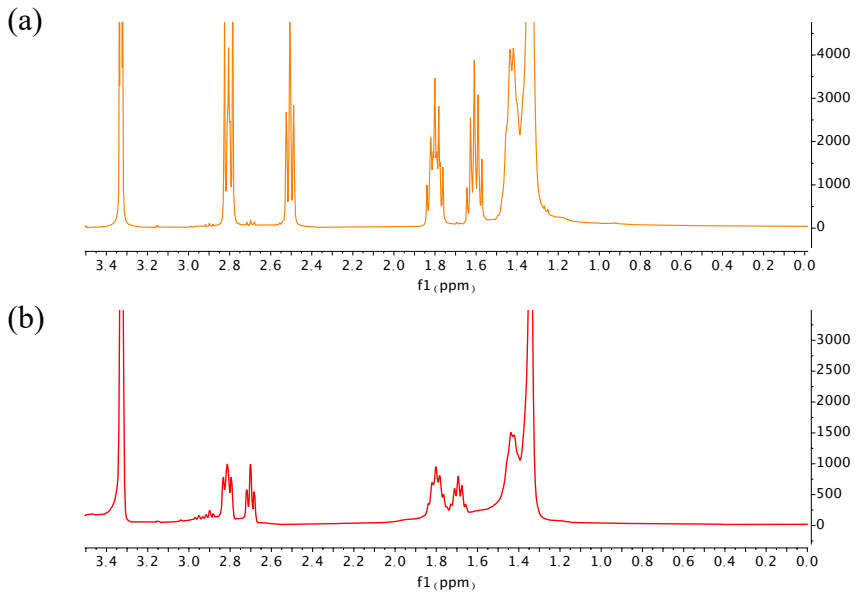

Figure 14: NMR spectra of (a) pure MUS in deuterated methanol and (b) etched MUS-coated gold nanoparticles in deuterated methanol.

The ^{1}H-NMR analysis is performed to control the purity of the prepared systems. In both cases, by comparing the spectra of the MUS-coated AuNPs with the pure MUS ligand it is evident the broadening of the peaks, which is caused by the assembly of the ligands on the nanoparticles. The absence of sharp peaks in the NMR spectrum obtained for the nanoparticle dispersions indicates a lack of impurities, such as unbound ligands. The structure modification of the capping groups and the formation of the Au—S bonding on the gold nanoparticle surface by removing one proton is responsible for the change in the chemical shift [16].

2.1.4 TEM Characterization

Transmission electron microscopy (TEM) allowed us to determine the size and the morphology of the nanoparticles. The preparation of the samples consisted in placing a drop of 4 μL of very diluted MUS-coated AuNPs dispersion (around 0.1 mg/mL) on a carbon film 400 Mesh copper grid and letting it dry for about one hour before the analysis. The images are recorded and acquired using a Talos L120C (120kV) microscope equipped with a Ceta S 16M CMOS camera (4k x 4k). The software ImageJ is used for the size distribution analysis. The mean nanoparticle diameter is 3.0 nm and the standard deviation is 0.5 nm (Figure 15).

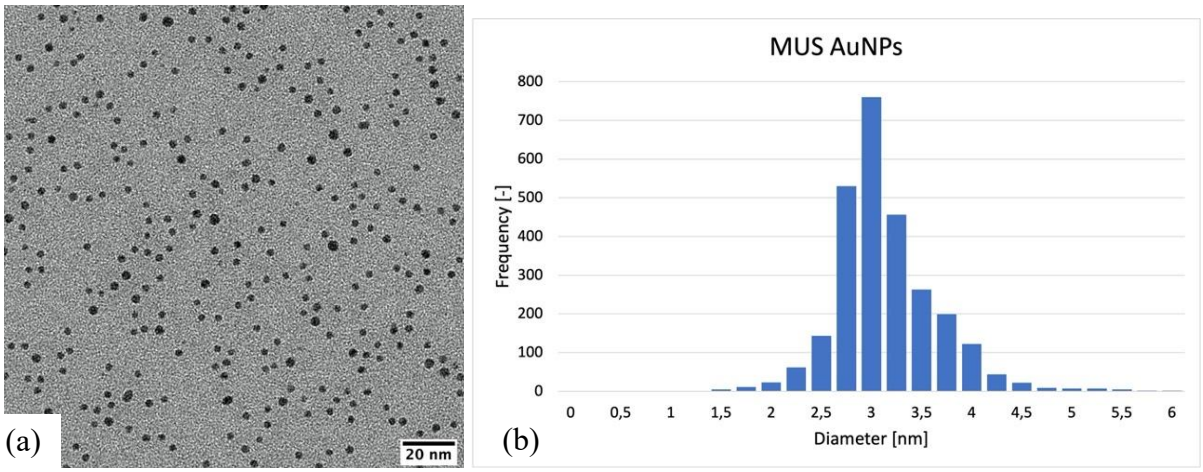

Figure 15: (a) TEM image and (b) size distribution of MUS-coated AuNPs, where $d_m = 3.0 \pm 0.5$ nm.

2.1.5 Dynamic Light Scattering and Zeta Potential measurements

The dynamic light scattering (DLS) analysis and zeta potential measurements are performed using the ZetaSizer Nano from Malvern Instruments.
The DLS is conducted as support measurement to the TEM analysis to determine the size of the nanoparticles.
Both measurements are conducted at 25°C. The average value ζ = -20,7 mV for the MUS-coated AuNPs water dispersion, while for the MUS-coated AuNPs dispersion in 30 mM NaCl the average value for the zeta potential is ζ = -15,4 mV. The size number distribution obtained for the water dispersion is presented in Figure 16.

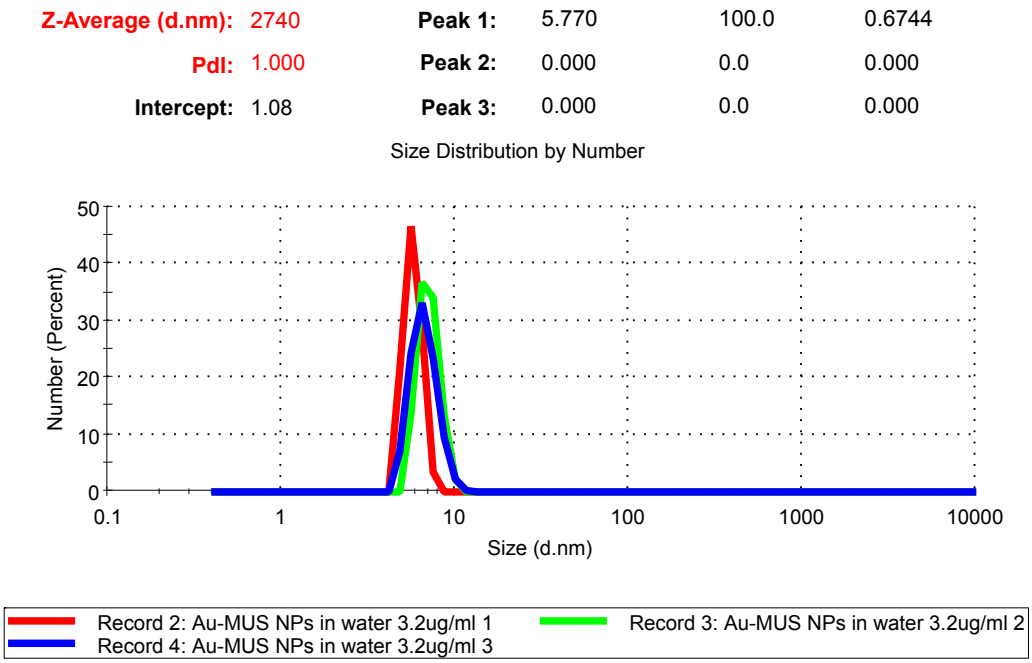

Figure 16: Number Distribution from dynamic light scattering.

2.2 Synthesis of PNIPAM-coated Gold Nanoparticles

The second part of this project is focused on a qualitative approach to study the effect of the temperature on the nanoparticle interactions. In order to be able to evaluate this temperature dependent behavior, poly(N-isopropylacrylamide) (PNIPAM) is used as a reference system and PNIPAM-coated gold nanoparticles are synthesized.
PNIPAM's specific properties make it one of the best and most reliable systems for testing and estimating the effect of temperature on the aggregation behavior and therefore the tunability of the interactions when there is a change in temperature. This behavior is investigated through the characterization by cryogenic transmission electron microscopy (Cryo-TEM).
PNIPAM is a water-soluble polymer with both hydrophobic and hydrophilic groups (Figure 17).

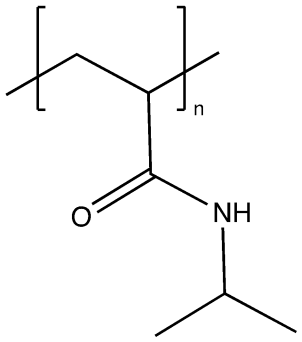

Figure 17: Poly (N- isopropylacrylamide), (PNIPAM).

It is one of the most studied temperature-responsive polymers, i.e. polymers which show a reversible volume phase transition when they are heated above a certain temperature (for pure PNIPAM it is around 32°C) in an aqueous medium [17].
This transition consists in going from a hydrophilic swollen state at lower temperature to a hydrophobic aggregated state at higher temperature, causing the loss of 90% ca. of its volume. This temperature is known as lower critical solution temperature (LCST) or volume phase transition temperature (VPTT) [18].
Its applications range from drug delivery systems, microgels, support for cell cultures, thermal imaging, sensing systems with manipulable solubility and controlled release of biomolecules such as proteins.
Below the lower critical solution temperature, the PNIPAM in the solution creates hydrogen bonds with the water molecules, causing it to absorb water and it becomes soluble because of the solvated side chains. Instead, upon heating, hydrophobic interactions are dominant. Hydrogen bonding is still present, but it is only between side chains of PNIPAM itself and the only groups exposed are hydrophobic, causing the PNIPAM to release water and phase separate, minimizing the surface area with the water. Thus, it becomes insoluble and it precipitates from the dispersion (Figure 18) [19].

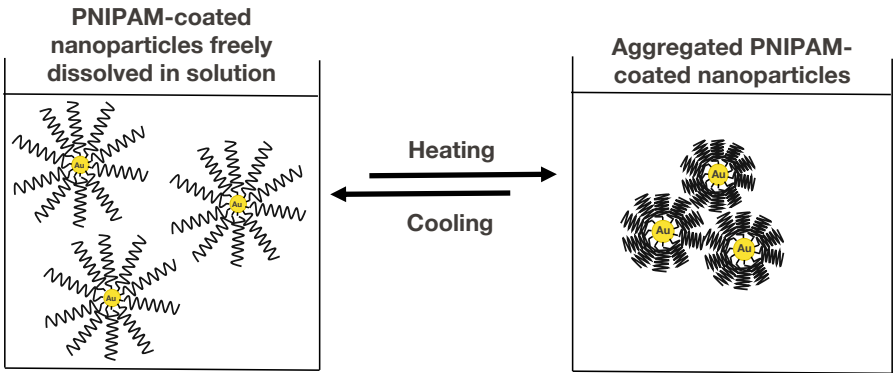

Figure 18: Thermo-responsive behavior of PNIPAM AuNPs.

The synthesis of PNIPAM-coated gold nanoparticles follows the same two-step procedure of the MUS-coated AuNPs previously described. After the production of oleylamine-coated gold nanoparticles, the PNIPAM-coated gold nanoparticles are obtained once again through the ligand exchange reaction with thiol-functional PNIPAM, as reported in Figure 19. For this part of the research, two PNIPAM thiols are used: 3 kDa and 6 kDa of molecular weight.

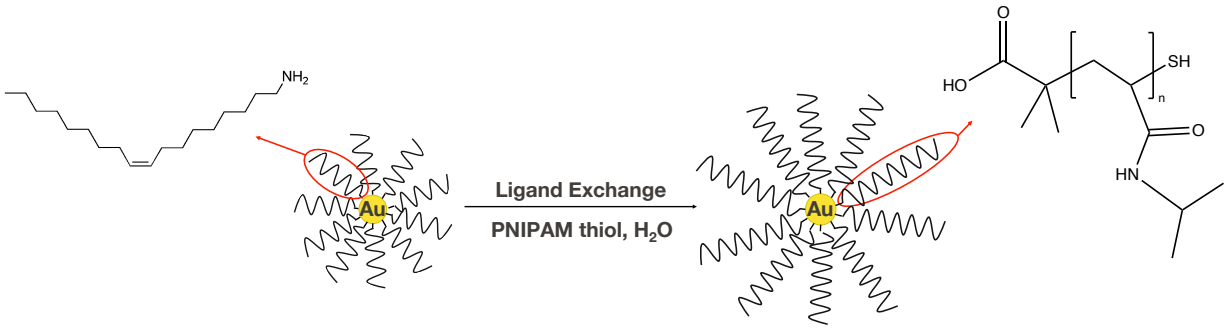

Figure 19: Ligand exchange reaction from OAm-coated AuNPs to PNIPAM-coated AuNPs.

Ligand exchange reaction is in general the same as previously described in subsection 2.1.2: oleylamine-coated gold nanoparticles are suspended in dichloromethane, and the PNIPAM ligands are dissolved in water phase. At the end of the reaction, the nanoparticles should be fully coated with PNIPAM ligands and should change phase from dichloromethane to water. Oleylamine ligands should still be dispersed in DCM. But, when conducting the ligand exchange reaction at room temperature, both of these phases are white, which implies that the nanoparticles are in neither of them, but instead they are trapped at the interface. In order to improve the ligand exchange, the flask containing the mixture is immersed in an ice bath. After decreasing the temperature, an immediate and clear change in solubility is visible, which suggests effective ligand exchange reaction (Figure 20).

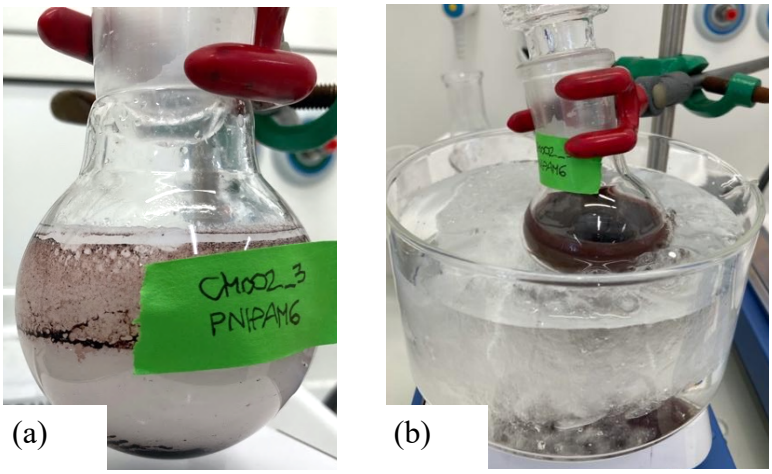

Figure 20: Ligand exchange reaction of PNIPAM-coated AuNPs (a) before and (b) after the immersion in the ice bath.

The next step is the purification of the PNIPAM-coated gold nanoparticles to remove the excess of both ligands. The first purification steps are sedimentation and filtration in water but in both cases the purification seems to be ineffective. The supernatant is still very foamy, implying the residual free ligands. The next method used is dialysis, first in water and then in dimethyl sulfoxide (DMSO), with a total of 7 changes in water and 4 changes in DMSO. Dialysis is a technique based on the diffusion of a solute from a higher concentrated solution to a lower concentrated solution of the solute through a semipermeable membrane until equilibrium is reached. A regenerated cellulose membrane of 8 kDa molecular weight cut-off is used in water while a regenerated cellulose membrane of 50 kDa molecular weight cut-off is used for the dialysis in DMSO. The nanoparticle dispersions are then recovered from the dialysis bags and subjected to final washes in water using the Amicon® Ultra-15 centrifugal filter devices (30k molecular weight cut-off), in order to freeze-dry them and obtain the nanoparticles' powder.

2.2.1 ^{1}H-NMR Characterization

Nuclear magnetic resonance spectroscopy measurements are carried out for pure PNIPAM 3kDa and PNIPAM 6kDa as well as for both PNIPAM 3kDa AuNPs and PNIPAM 3kDa AuNPs in deuterium oxide (D_2O). The ^{1}H-NMR spectra for these systems are presented in Figures 21 and 22, respectively.
For both of the nanoparticle dispersions the peaks appeared broad, confirming the efficacy in the purification and washing process.

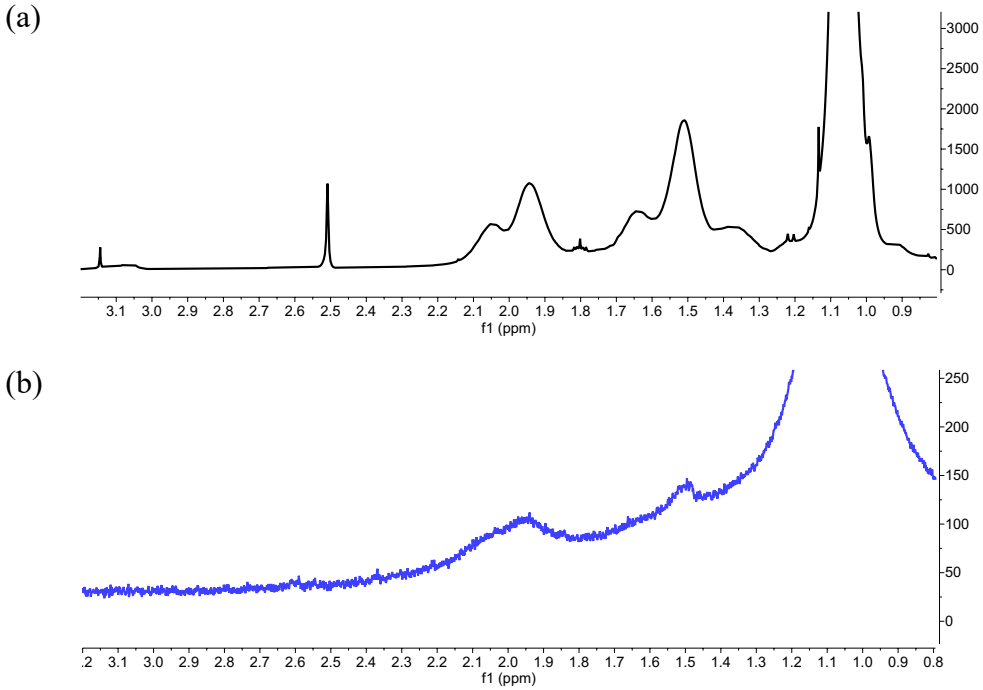

Figure 21: NMR spectra of (a) pure PNIPAM 3kDa in deuterium oxide and (b) non-etched PNIPAM 3kDa gold nanoparticles in deuterium oxide.

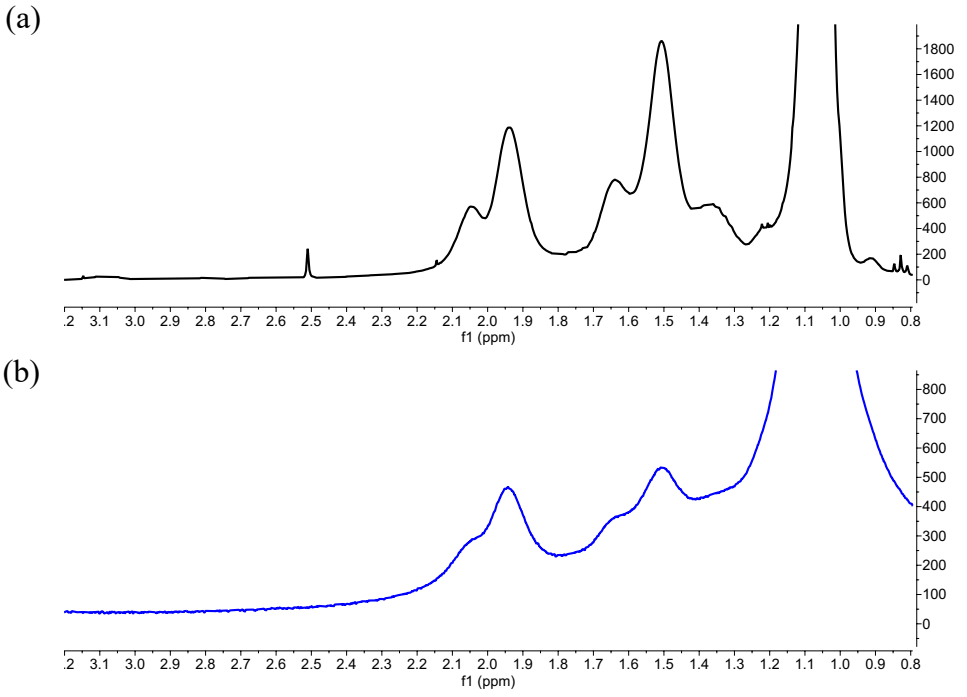

Figure 22: NMR spectra of (a) pure PNIPAM 6kDa in deuterium oxide and (b) non-etched PNIPAM 6kDa gold nanoparticles in deuterium oxide.

2.2.2 TEM Characterization

The transmission electron microscope is used to obtain the images and the size distributions for the PNIPAM 3 kDa and PNIPAM 6 kDa gold nanoparticles respectively as shown in Figures 23 and 24. The experimental details are the same as subsection 2.1.4 described previously. Both of them appeared to be very well dispersed, in particular the PNIPAM 3 kDa AuNPs have a mean diameter d_m = 2.8 nm and the standard deviation is 0.4 nm, while the PNIPAM 6kDa gold nanoparticles are slightly bigger than the previous ones, their mean diameter is d_m = 3.2 nm and the standard deviation is 0.4 nm.

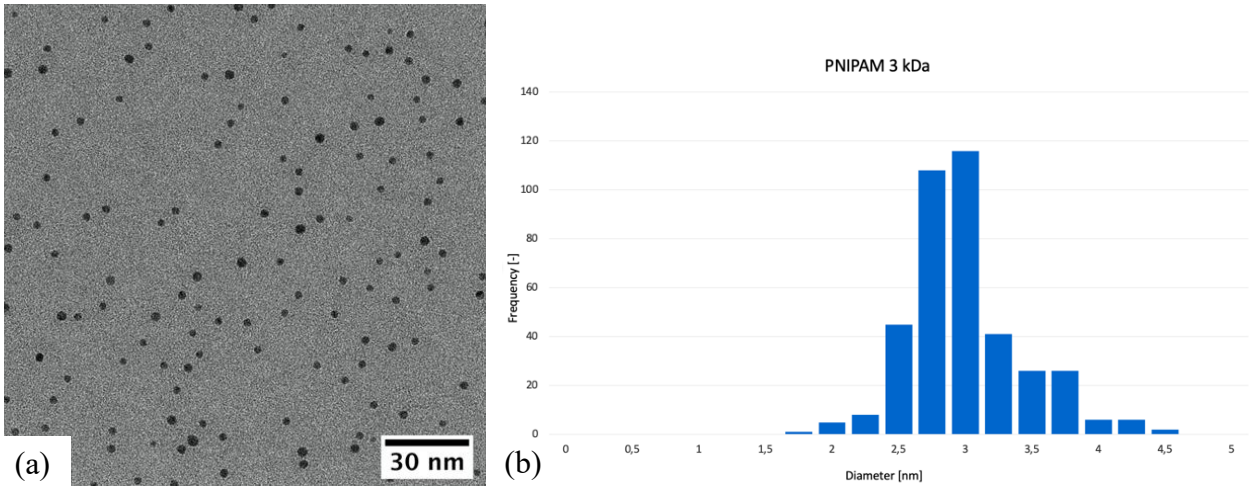

Figure 23: (a) TEM image and (b) size distribution of PNIPAM 3kDa AuNPs, where $d_m = 2.8 \pm 0.4$ nm.

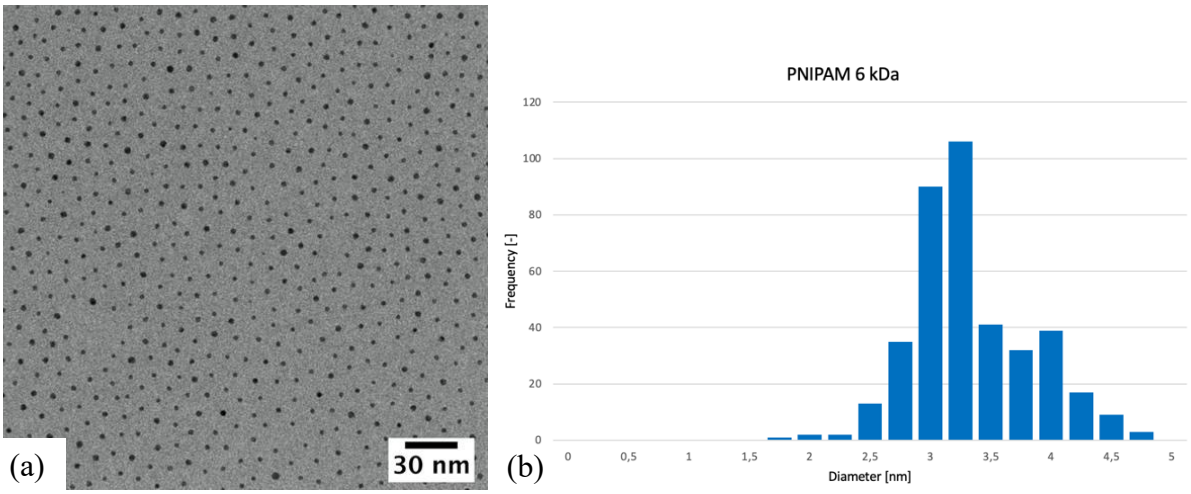

Figure 24: (a) TEM image and (b) size distribution of PNIPAM 6kDa AuNPs, where $d_m = 3.2 \pm 0.4$ nm.

3. Methods

3.1 Cryogenic Transmission Electron Microscopy Tomography (Cryo-ET)

Cryogenic transmission electron microscopy tomography (Cryo-ET) is a technique that falls under the transmission electron microscopy tomography that analyzes the samples at cryogenic temperatures.
In 2017 Jacques Dubochet, Joachim Frank and Richard Henderson won the Nobel Prize in Chemistry for their studies and contribution in the development of this technique.
It is used in this project in order to deliver density maps of the nanoparticles near the atomic resolution (about 1.5 Å) and to characterize the nanoparticles interactions. The peculiarity of this technique is that it allows the direct observation of colloidal systems and biomolecules in their native state, with the specimen that is cryogenically conserved [20].
This is obtained by preparing the sample in a vitrified, frozen-hydrated state through the fast immersion and freezing of the sample first in liquid ethane and later liquid nitrogen that causes the formation of an amorphous ice layer. Liquid ethane is used in the freezing process because of its higher heat capacity and because the temperature at which ethane is liquid is a little above the one of liquid nitrogen [21]. The microscope used for this project is the Thermo Fisher Talos L120C G2 transmission electron microscope (Figure 25) for both ambient and cryogenic 2D sample imaging and the Tecnai F20 microscope for the 3D tomography (with +/- 60° tilt angle) that are located in the Interdisciplinary Centre for Electron Microscopy (CIME) facility at EPFL.

Figure 25: The Talos L120C G2 transmission electron microscope located in the CIME facility at EPFL.

The main component of the cryogenic microscopy is the specific cryogenic holder where the grid embedded with the vitrified sample is kept during the analysis [22]. The cryo-holder is kept in vacuum prior to its cooling with liquid nitrogen and its insertion in the microscope (Figure 26).

Figure 26: Cryo-ET holder kept under vacuum in the Turbo Pumping Station Gatan, model 655.

3.1.1 Transmission electron microscopy operating principle

The cryogenic transmission electron microscopy tomography is an extension of the transmission electron microscopy (TEM) and it relies on the same operating principles. High voltage (around 120kV-200kV) is applied to an electron source that consists of a lanthanum hexaboride LaB_6 or tungsten filament while operating in a high vacuum. From this, electrons are emitted and the electron beam is accelerated by electromagnets. The beam penetrates and interacts with a very thin sample (in our case a dry nanoparticle dispersion on a grid). The interaction between the electrons creates an image that, because of the electromagnetic lenses, is magnified and projected on a fluorescent screen and detected by a sensor such as a charge-coupled device (CCD) camera (Figure 27).

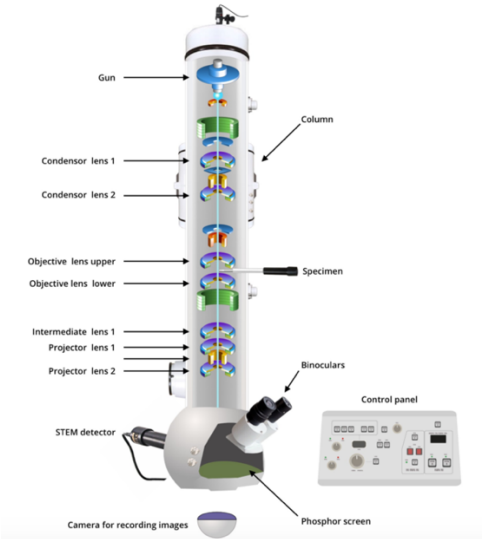

Figure 27: General profile of a transmission electron microscope describing the internal components [23].

3.1.2 Cryo-ET Sample preparation

The preparation of the sample for the Cryo-ET characterization is a crucial and very important step for a good quality analysis and imaging. The sample consists of a 3-5 μL nanoparticle dispersion that is deposited onto a grid made out of a conductive material, like copper, covered with a carbon film. The grid is quickly frozen into liquid ethane and stored in liquid nitrogen where the water solidifies and forms an amorphous ice layer. There are several kinds of grids that can be utilized for the Cryo-ET characterization and they differ in the type of carbon support film. This carbon film can in fact have regular mesh and is called Quantifoil Holey Carbon film with circular, square or multi arranged holes (used for the 3D tomography), or have irregular holes distribution such as the Holey Carbon film and the Lacey Carbon film. The type of grid mostly depends on the hole size on the carbon film, which is influenced by the degree of magnification used for the analysis.
These grids are hydrophobic, hence, before they are covered with the nanoparticle dispersion, they undergo a glowing discharge process using the ELMO Glow Discharge System (Figure 28). This process consists in the removal of adsorbed hydro-carbons on the carbon film and in making the surface negatively charged, so the grid goes from being hydrophobic to hydrophilic and therefore allows the nanoparticle dispersion to better spread on the grid [24].

Figure 28: ELMO Glow Discharge System used for the Cryo-ET grid hydrophilization.

It is important to utilize the glow discharged grid at least half an hour after the treatment because the longer the time between the glow discharge and the preparation of the sample, the more the higher reactive groups that are present of the carbon surface, such as oxygen radicals, are going to turn to less reactive ones, like carbonyls [25].
The instrument used for the Cryo-ET sample preparation is the FEI Vitrobot Mark IV (Figure 29).

Figure 29: FEI Vitrobot Mark IV used for the Cryo-ET sample preparation.

After the deposition of the nanoparticle dispersion, the grid is inserted in a climate chamber at set temperature and relative humidity with the help of tweezers. Meanwhile, the cryo-container with the Cryo-ET grid boxes that will store the samples is first filled with liquid nitrogen. Once all the components are at liquid nitrogen's temperature (which can be evaluated by the absence of bubbles), liquid ethane is added into a bronze cup in the middle of the container (Figure 30).

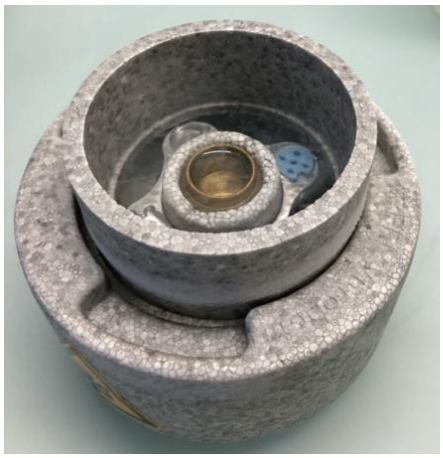

Figure 30: Container for liquid nitrogen and liquid ethane (in the bronze cup); it contains the Cryo-ET grid blue box where the samples will be stored.

This container is placed at the bottom outside of the climate chamber. The grid is immediately blotted (pressed from both sides by a blotting device at a set blotting force) using Whatman

ashless filter paper and this has the purpose of creating a thin homogeneous film of the nanoparticle dispersion. The blotting step is illustrated in Figure 31.

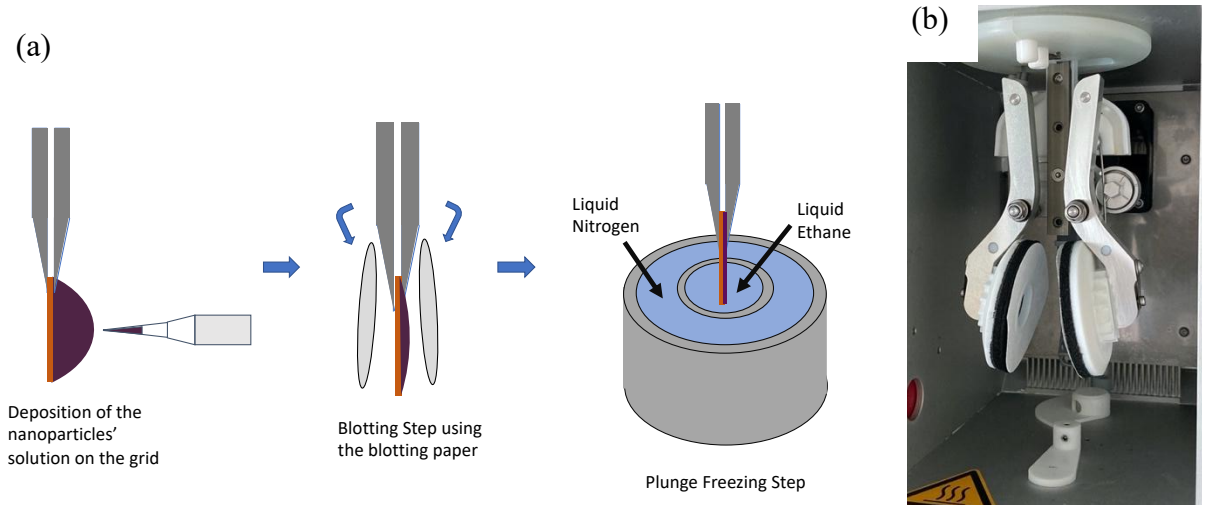

Figure 31: (a) Blotting step in the Cryo-ET sample preparation. (b) Blotting device in the climate chamber of the Vitrobot.

After the blotting step, the grid is quickly immersed in the bronze cup containing liquid ethane where the water instantly freezes, and the formation of ice crystals is prevented. It is then rapidly transferred to the liquid nitrogen on the side and stored in the Cryo-ET box before analyzing it with the microscope. The ice thickness has to be optimized in order to obtain a good reliable sample: a thick ice layer can cause multiple scattering of the incident electrons and decrease the quality of the image; in the limit case, the ice is too thick that the electron beam is not able to penetrate it. The formation of a vitreous layer of ice is the fundamental step in the Cryo-ET and keeps the nanoparticles in a native state. The amorphous ice layer with suspended nanoparticles has to remain at the liquid nitrogen's temperature while it's stored and analyzed in the microscope to avoid any phase changes to other kinds of ice that prevent high-quality imaging. When working in these conditions, a lot of challenges can be faced during the sample preparation, like its manipulation, the grid transfer and the imaging. For example, if the grids are exposed to room atmosphere, frost might form on the grid itself and the ice crystals can ultimately block the electron beam. Other contaminations can be present that can alter the quality of the grids and the imaging. If during the sample preparation the freezing is not rapid enough, it can cause the creation of hexagonal ice, and if the sample heats up it can cause devitrification that instead leads to the formation of cubic ice.
When analyzing these samples in the microscope, because of their extreme susceptibility to radiation damage, low-electron dose conditions are used in order to minimize the sample damage before the image acquisition. First, the areas of interest are identified at low magnification or dose, then a near-by area is focused at high magnification and finally the image of the interested feature at high magnification is acquired [20].

3.1.3 Cryo-ET of nanoparticle dispersions

The images of the nanoparticles that are randomly oriented in the vitrified ice layer acquired from the cryogenic microscope depend on the interactions between the nanoparticles and the electron beam. During the analysis with the microscope, the 2D images are acquired at 200kV with a magnification of 50.000x (0.2nm of image resolution) for each orientation using the Tecnai F20 microscope where the computer distinguishes the tilt-series from –60° to +60° (with an increment of 2°) to calculate the 3D volume. The image contrast given by the gold nanoparticles allows to perform the image segmentation via intensity threshold directly to the 3D images and identify the nanoparticles. The reconstruction is performed with the simultaneous iterative reconstruction technique (with 24 interactions). The Cryo-ET workflow is shown in Figure 32.

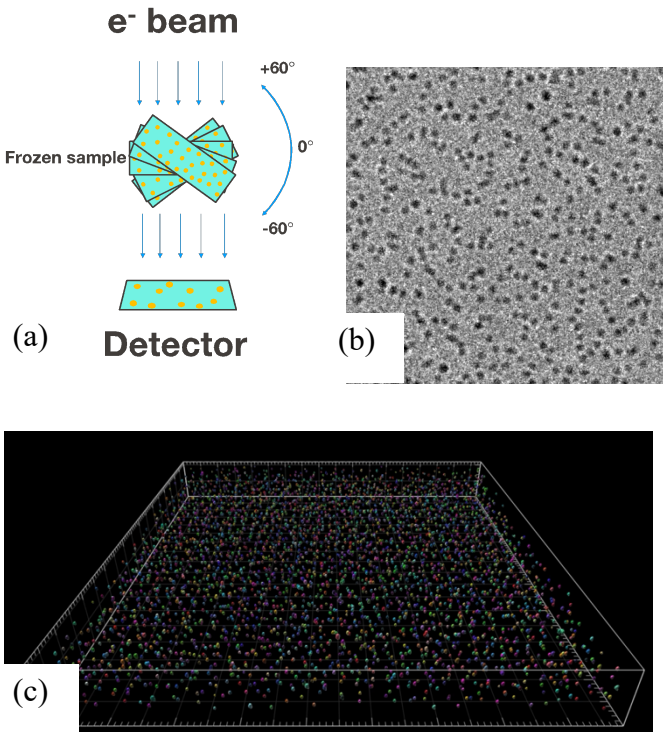

Figure 32: (a) Tilt-series and (b) processing of images alignment
(c) 3D reconstruction [Images by Dr. Quy Ong Khac]

3.1.4 Advantages and Disadvantages of Cryo-ET

In Table 1 are summarized the main advantages and disadvantages of the cryogenic transmission electron microscopy tomography [21].

Advantages	Disadvantages
- The sample contains information about the structure which reflects its native state - A wide range of biomolecules and particles can be characterized - Different kinds of specimen such as protein complexes, viruses, cells, can be observed - Little amount of the sample is required - High Resolution (1.5-2 Å) - Reconstruction can be performed with few particles - Damage to the sample by the electron beam can be limited with the use of the low dose technique - Crystallization of the molecules is not required, thus the structure is not modified - Biomolecules are frozen and are observed in all their different conformations	- The signal to noise ratio is very low - Problems with image contrast - The cross section of the vitrified sample complicates the image acquisition when dealing with tilted specimen - During slow sample freezing, cubic ice can form, so the plunging has to be very quick in order to obtain good quality images. - The penetration of the electron beam depends on the ice and sample thickness and is influenced by the mean free path (it is around 500 nm for 300 kV microscope) - The nanoparticles' distribution is affected by the preparation of the sample, that can be corrected with automation - Very expensive technique - Limit on the molecular weight (38 kDa ca.) - The electron dose supported by the specimen is limited and it is due to the damage caused by the radiation, which is influenced by the voltage and sample characteristics [26].

Table 1: Summary of the main advantages and disadvantages of the cryogenic transmission electron microscopy tomography [27].

3.2 Small Angle X-ray Scattering (SAXS)

Small angle X-ray scattering is used in this project to compare and validate the nanoscale structures obtained by high-resolution methods like the cryogenic electron transmission microscopy tomography. The SAXS experimental measurements were carried out by Dr. Neda Iranpour Anaraki from Empa's Center for X-ray Analytics in St. Gallen, Switzerland, with who we collaborated in this project for the scattering characterization.
SAXS is a lower resolution method that exploits the long-range distance and shape of the nanostructure and the interactions between a wide size-range of the nanoparticles or biomolecules. It is an accurate, non-destructive method that requires a minimum for the sample preparation process.
The SAXS measurement consists in a sample containing the nanoparticle dispersion being exposed to an incident collimated primary beam of X-rays of a defined wavelength (0.05-0.5 nm ca.) at small angles, about 0.1-5°. The interaction with the sample creates scattered secondary waves that are later registered on a detector and the SAXS profiles are analyzed after being radially averaged (Figure 33) [28].

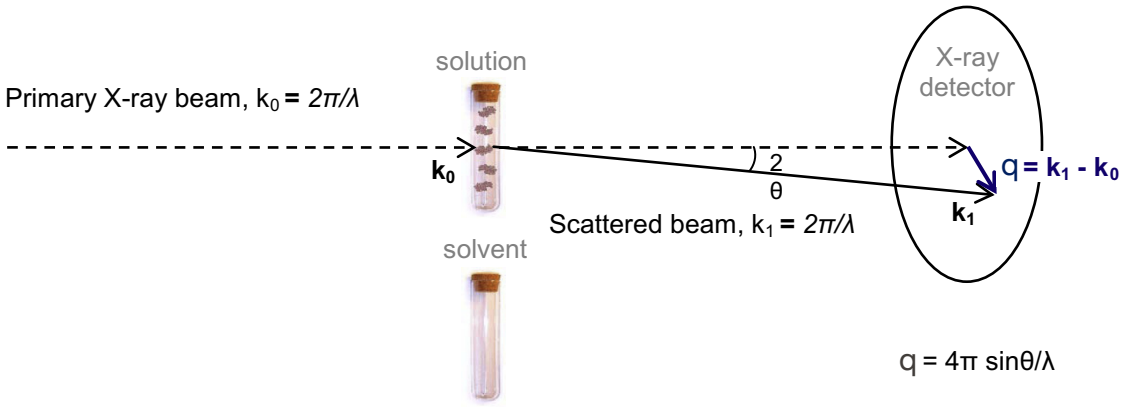

Figure 33: Small angle X-ray scattering experiment: an incident collimated primary beam interacts with a capillary sample containing the nanoparticle dispersion [29].

The instrument used is a Bruker Nanostar with a 300 μm beam diameter in which the measurements are conducted at room temperature and in vacuum (around 10^{-2} mbar).
The main scattering process is elastic and is characterized by the absence of energy transfer between the incident beam and scattered beam and the assumption that the scatterers (i.e. the nanoparticles) are fixed in space. Other processes like the Compton and Raman scattering contribute mostly to the background (e.g. solvent). In case of low contrast, usually when dealing with biomolecules and other biological systems, the beamlines have to be adapted in order to minimize the contribution of the background that can prevent good data acquisition. The

scattering of the X-rays depends on the number of nanoparticles present in the solution in the exposed volume, the nanoparticle's size and it is proportional to the scattering length density.
The derivation of the thermodynamic parameters directly from the reciprocal space, such as the molecular mass, radius of gyration (R_g, it is a measure of the compaction of the nanoparticle), and the nanoparticle's diameter, is obtained by the profiles after the subtraction of the background scattering. These parameters give information about the size, distribution and shape of the nanoparticles or biomolecules in the solution [30].
From the SAXS data, by using the inverse Fourier transform, one can obtain the real space data. The typical curve of the scattering intensity obtained from the SAXS experiment is reported in Figure 34.

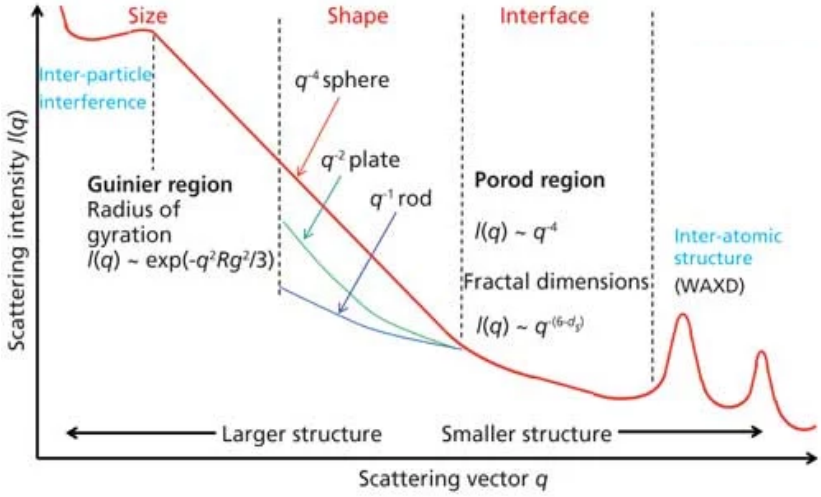

Figure 34: Theoretical SAXS profile [31].

The nanoparticles produce a scattering intensity I(q) as a function of the modulus of the scattering vector **q,** which depends on the size of the beam and the beamstop:

$$|\vec{q}| = \frac{4\pi \, sin\,(\theta)}{\lambda} \tag{4}$$

$$I(q) = \, < A(q) \cdot A^*(q) >_{\Omega} \tag{5}$$

where 2θ is the scattering angle between the primary and the secondary beam, λ is the wavelength, $A(q)$ is the scattering amplitude (which is calculated through the Fourier transform of the scattering length density) and Ω represents the different orientations over which I(q) is averaged [30]. The profile of the scattering intensity is affected by the distribution, size and shape of the particles in the solution. Different regions can be identified: the Guinier region, which provides information on the quality of the sample and the calculation of R_g, and the Porod region for large values of the scattering vector. In case of liquid-like nanostructures, the interference effects that are caused by the spatial correlation are taken into account by the structure factor S(q), which is measured as a function of the scattering vector [32].
The structure factor analyzes the interference of the scattered beam and the correlations that depend on the interactions with the nanoparticles and it gives a measure of local correlations of the system. The profile of the structure factor is influenced by the nanoparticles' number

concentration, the intensity and their interactions [33]. Strong attractive or repulsive interactions between the nanoparticles can influence the scattering intensity and thus the different parameters that can be derived from the curve. The repulsion between nanoparticles decreases the scattering intensity. In order to assess the contribution of the interactions between the nanoparticles to the I(q), different concentrations of nanoparticle dispersions are analyzed [30]. The scattering intensity I(q) is proportional to S(q) and $|F(q)|^2$, where F(q) is the form factor that indicates the size and shape of the nanoparticles [34].
A disadvantage of the SAXS technique is that any sample, whether monodisperse or polydisperse, will yield the data, therefore the absence of artifacts is provided by the correct analysis of the scientist and it is his responsibility to find the correct solution [35].

3.2.1 SAXS Sample preparation

The usual protocol for the sample preparation used in the Small Angle X-ray Scattering experiment follows a protocol [28]:

- A needle is used to extract between 5-30 μL of the sample containing the nanoparticle dispersion.
- A quartz capillary tube (with a maximum diameter of 2.2 mm, in our case 1.5 mm) is filled with the sample.
- The capillary tubes are sealed by melting some wax on the top part.
- The tubes are then placed and secured onto the sample holder (Figure 35).
- The holder containing the different samples is inserted back into the chamber and vacuum is performed.

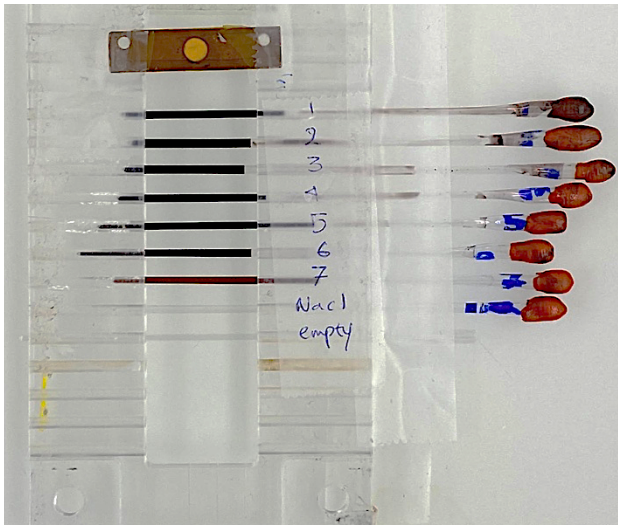

Figure 35: Capillary sample containing the nanoparticle dispersions at different concentrations together with the two pure solvents used to perform the SAXS measurement [Image by Dr. Neda Iranpour Anaraki].

4. Results and Discussion

4.1 Effect of Concentration and Presence of Salt on MUS-coated gold nanoparticles interactions

4.1.1 Nanoparticle number density from Cryo-ET

From the Cryo-ET characterization, the volume of the sample, the number density of nanoparticles and their coordinates can be calculated. In Figure 36 are reported the number densities ρ of the nanoparticles at different concentrations in Milli-Q water and in NaCl 30mM dispersions. The nanoparticle number density indicates the number of nanoparticles per unit volume and gives information about the concentration of the discrete systems.

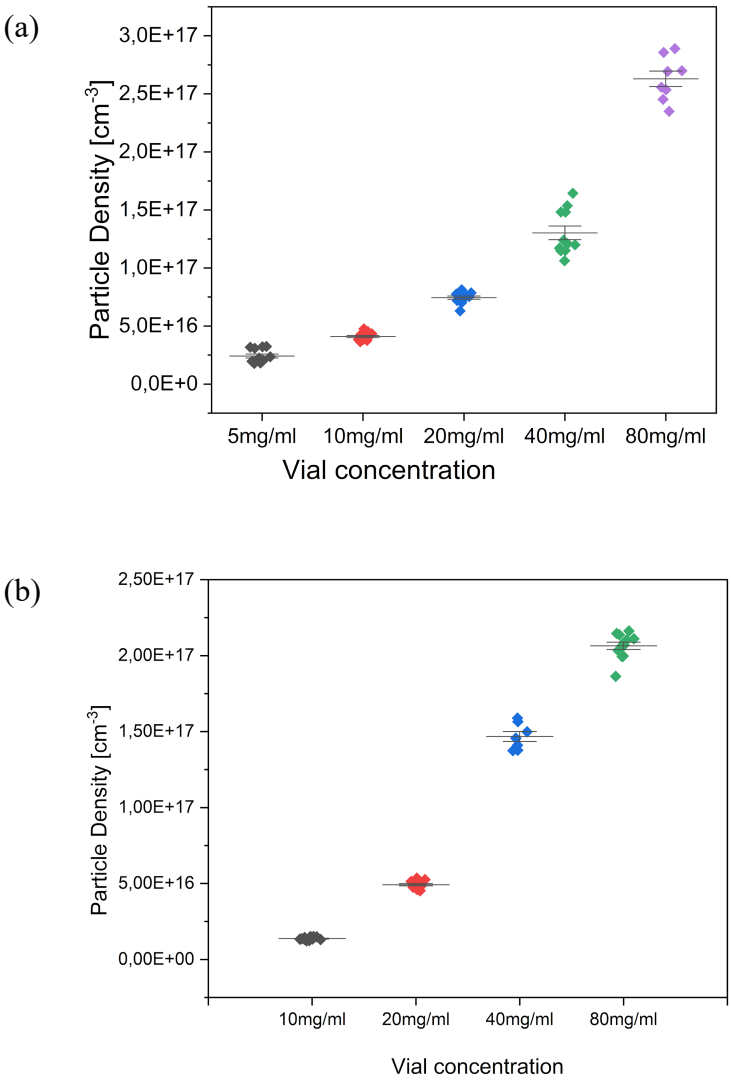

Figure 36: (a) Nanoparticle number density in water solution and (b) in 30 mM NaCl solution for the different nanoparticle concentrations.

4.1.2 Radial distribution function from Cryo-ET

The 3D maps of the nanoparticles experimentally derived from the Cryo-ET tomograms are analyzed using an analytical approach. The coordinates of the center of gravity of the nanoparticles are used to determine and compute the radial distribution function g(r) through an analytic algorithm, in order to quantitatively evaluate the nanoparticles' positions in the three dimensions. The g(r) describes the local density of the nanoparticles at a distance r from a nanoparticle at r + dr. It is equal to 0 for very short distances (that is because two particles cannot occupy the same volume) and it tends to unity at large distances where correlations are no longer significant. It is often referred to as the pair distribution function. The algorithm for the 3D g(r) computation proposed by Kopera and Retsch (2018) has been taken as a reference in this work [36]. They make use of the intersection volume between the sample and a spherical shell for the purpose of correctly normalizing g(r) and constraining the maximal radial distance by the overall dimensions of the sample, so as to have lower noise and good long-range particle correlations.

4.1.2.1 g(r) of MUS-coated gold nanoparticles in water

The data of g(r) as a function of the interparticle distance obtained from the Cryo-ET analysis are reported in Figure 37. The curves differ in the nanoparticle concentration in the solution. The concentrations chosen for the measurements are, in ascending order, 5, 10, 20, 40 and 80 mg/mL.

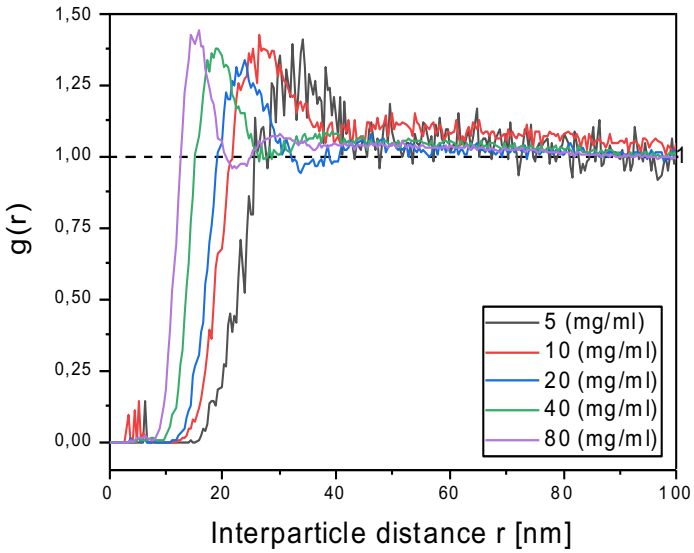

Figure 37: Radial Distribution Function g(r) of MUS-coated AuNPs in H_2O at different concentrations from Cryo-ET analysis.

As seen in the plot, the peak in the radial distribution function, which expresses the highest probability of finding near nanoparticles, is found at lower separation distance between the nanoparticles for more concentrated dispersions i.e. 80 mg/mL and is of the order of 15 nm.

For lower concentrations, the position peak shifts at a higher distance. Thus, the probability of finding a particle at a closer radial distance when there is a particle at the origin is higher for high nanoparticles concentrations [37].
The short peaks that can be found for small interparticle distances are related to the nanoparticles that are found in aggregation state such as dimers, trimers, since the distance between them is shorter than the set limit threshold interparticle distance, in our case it has been defined as the mean diameter of the nanoparticle summed with double the length of the MUS ligand.

4.1.2.2 g(r) of MUS-coated gold nanoparticles in 30mM NaCl

When salt is added in the solution, the dissociated counterions screen the electrostatic repulsions between the nanoparticles and this phenomenon can be described through the theory by Gouy-Chapman for the electric double layer. The profiles of the radial distribution function are reported in Figure 38 for different nanoparticle concentrations. The number density of the 5mg/mL solution was found to be approximately the same as the one for the 10mg/mL nanoparticles' solution in NaCl 30 mM. The concentration of 5 mg/mL is not reported because of the lower nanoparticle count (lower concentration) that causes noisier data and doesn't provide good quality analysis.

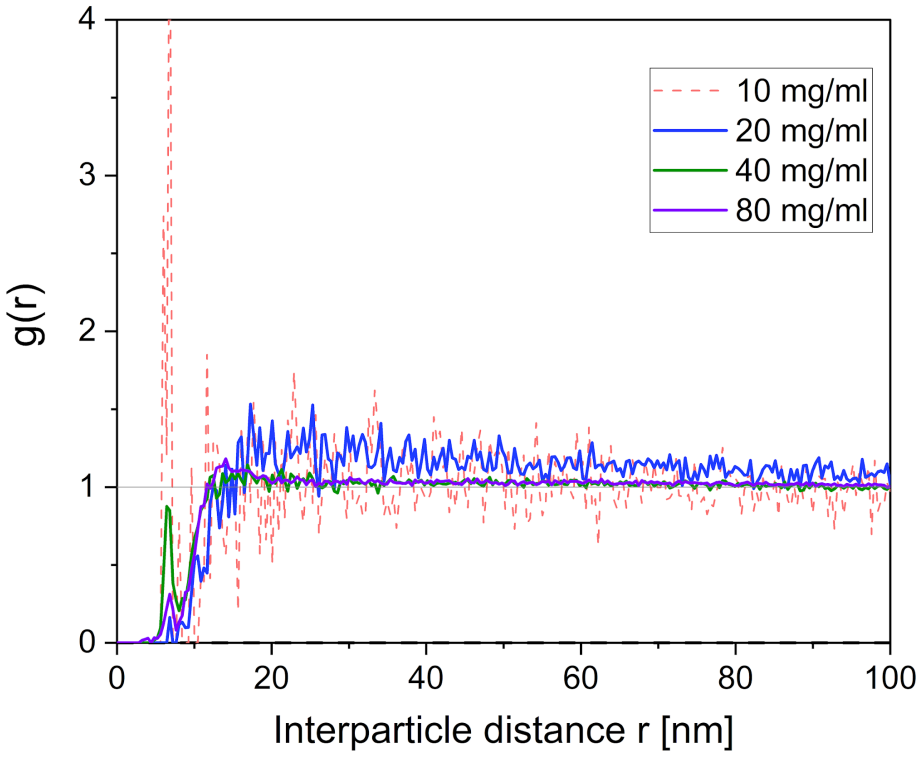

Figure 38: Radial Distribution Function g(r) of MUS-coated AuNPs in 30 mM NaCl at different concentrations from Cryo-ET analysis.

At high concentrations, the shift is visible thanks to the higher nanoparticle count. Already starting from the 20mg/mL concentration the g(r) curve goes even above the unity.

4.1.3 Potential of mean force from Cryo-ET

From statistical mechanics, the effective interaction between the nanoparticles is related to the radial distribution function and it can be calculated by the potential of mean force or interparticle interaction potential U(r)

$$U(r) = -k_B T \, ln \, g(r) \tag{6}$$

The potential of mean force contains information and contribution from many-body interactions.

4.1.3.1 U(r) of MUS-coated gold nanoparticles in water

The interaction potentials U(r) calculated at different concentrations for MUS-coated gold nanoparticles dispersed in water are illustrated in Figure 39.

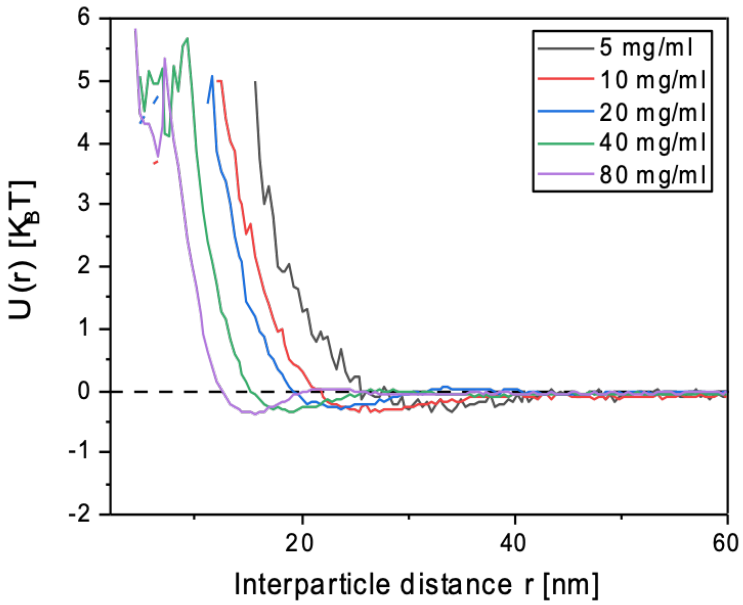

Figure 39: Interaction potential U(r) of MUS-coated AuNPs in H_2O at different concentrations from Cryo-ET analysis.

When comparing the two graphs of g(r) and U(r), the maximum of the radial distribution function is located at the distance of the secondary minimum of the interaction potential U(r), for each concentration respectively. Therefore, the local concentration of particles around a specific particle becomes very high in the proximity of the secondary minimum. That shows that the interaction between the nanoparticles is responsible for the structure of the fluid [38].

The energy jump barrier is lower for low concentrated dispersions. The shallow secondary well for low concentration can be detected at a higher interparticle distance. Coagulation in the secondary minimum is also known as reversible coagulation. As opposite to the primary minimum, where the nanoparticles can get into intimate contact and the aggregation is irreversible, in the case of aggregation in the secondary well the nanoparticles are surrounded by a liquid film and the energy depth is smaller [39].
In water solution, the nanoparticles interact mostly due to the electrostatic repulsions between their surface charges [33].

4.1.3.2 U(r) of MUS-coated gold nanoparticles in 30mM NaCl

As introduced in the previous case, the plots for the potential of mean force for the different nanoparticle concentrations are obtained from the g(r) data. In the case of the solution with higher ionic strength, the long-range of the electrostatic repulsion decreases, as shown in Figure 40.

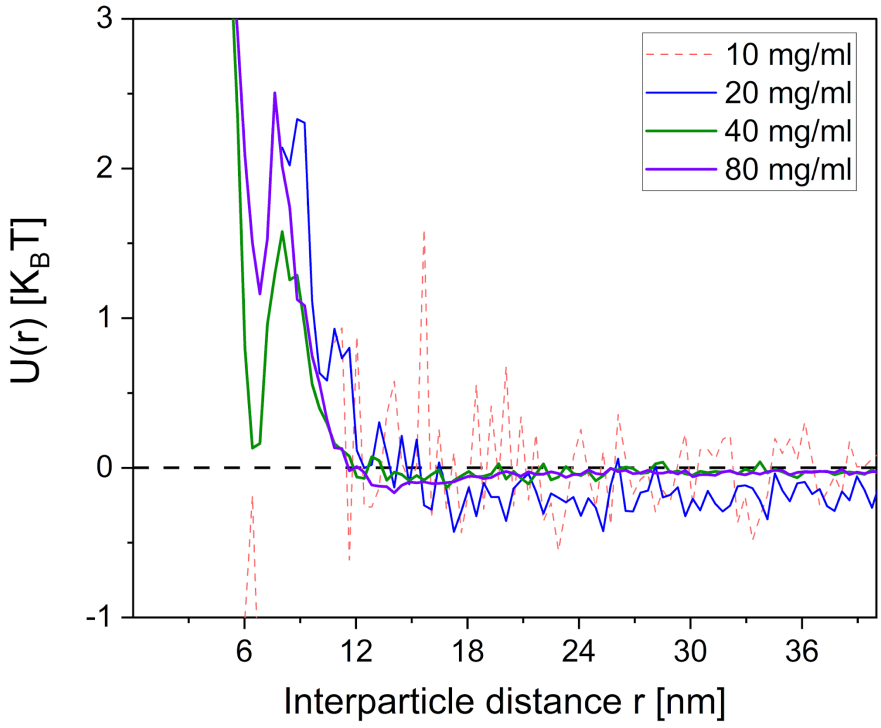

Figure 40: Interaction potential U(r) of MUS-coated AuNPs in 30mM NaCl at different concentrations from Cryo-ET analysis.

The potential of mean force curves as a function of the interparticle distance follow the same trend as for the water for different nanoparticle concentrations, i.e. the energy jump barrier is lower for low concentrations and the secondary well for low concentration is found at a higher interparticle distance, but the minimum is found at smaller interparticle distance because of the screened electrostatic interactions due to the presence of the salt.

4.1.4 Validation of Cryo-ET results by SAXS

The first goal of the project is to evaluate and compare the results obtained from the Cryo-ET and the ones obtained from the Small Angle X-ray Scattering.
The correspondence of the two techniques can prove that the freezing and vitrification process in the Cryo-ET analysis doesn't in fact modify the sample's properties, so the nanoparticles are characterized in their actual native state. The parameter investigated for the comparison is the structure factor S(q).
The procedure to obtain the experimental structure factor from Cryo-ET involves the transformation of the radial distribution function.
The structure factor is in fact related to the radial distribution function: S(q) can be calculated by the Fourier transform of the g(r). The maximum in the S(q) profile curve is positioned at a value of the scattering vector $q_{max} \approx 2\,\pi/r_{max,}$ that corresponds to the separation interparticle distance where the peak of g(r) is located [40].
The structure factor experimentally derived from the cryogenic transmission electron microscopy tomography can be compared with the one obtained from X-ray scattering analysis. Measurements for concentrations 80, 60, 40, 20, 10, 5, 1 mg/mL of MUS-coated gold nanoparticles in ultrapure water and 30mM NaCl dispersions are performed.
The data of the scattering intensity from the lowest concentration is used for the calculation of the form factor. From there, the structure factors are extracted and normalized to 1 at high values of the scattering vector and the data are manipulated using the software SasView.
The structure factor is calculated as a function of the form factor and the separation distance between two nanoparticles i and j by using the Debye scattering equation

$$S(q) = \sum_{i}^{N}\sum_{j}^{N} F_i(q)F_j(q)\frac{\sin(qr_{ij})}{qr_{ij}} \qquad (7)$$

The structure factors from the two techniques have been reported in one unique plot (Figure 41) so as to appreciate their comparison.

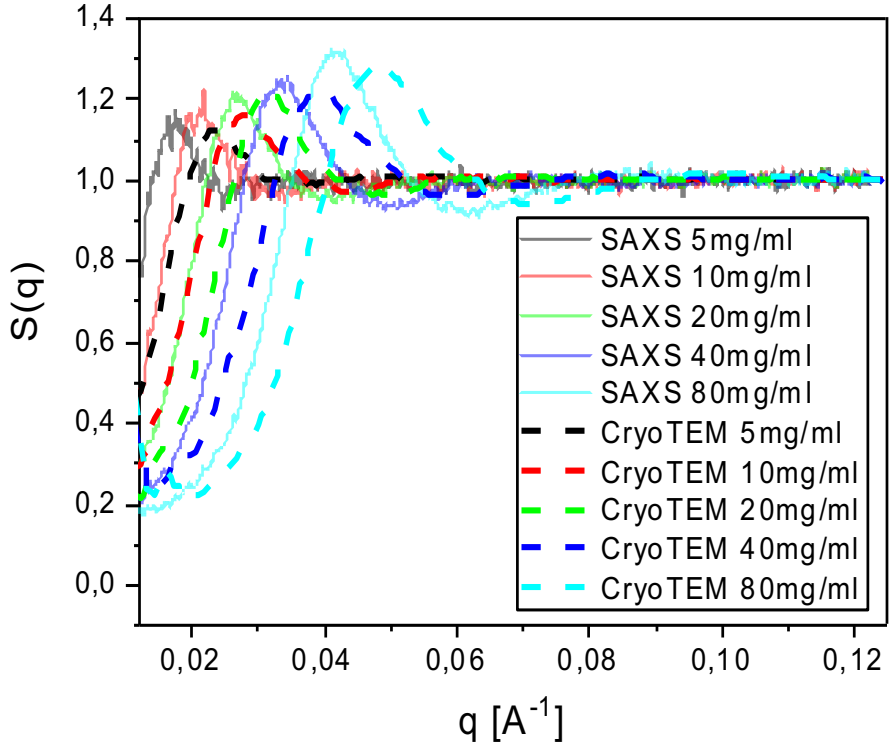

Figure 41: Structure factors S(q) of MUS-coated AuNPs in H_2O at different concentrations from Cryo-ET (dash lines) and SAXS (full lines).

At low values of the scattering vector q, the structure factor starts lower than 1, it reaches a maximum and then goes down to unity for each concentration. Such profiles are typical for describing the repulsion of the electrostatic interactions [41].
The peak position of the structure factor is located at higher values of the scattering vector for higher concentration of nanoparticles. It is clearly noticeable that the two sets of curves of the structure factors as a function of different nanoparticle concentrations in the dispersion follow the same trend: for each concentration, the S(q) of the two curves from Cryo-ET and SAXS are related and have pretty much the same intensity, but differ in a shift in the x-axis of the scattering vector q. The reason for this can be addressed to the difference in the concentration of the nanoparticles in the sample, probably due to the smaller sample volume that is operated in the Cryo-ET sample preparation. Therefore, a linear regression analysis is conducted. First, the positions of the peaks from the two techniques are correlated for each nanoparticle concentration. Later, the correlation peaks obtained are linearly fitted in a single plot where the equation of the straight line is derived, in this case y= 1.0051x + 0.00546 (Figure 42).

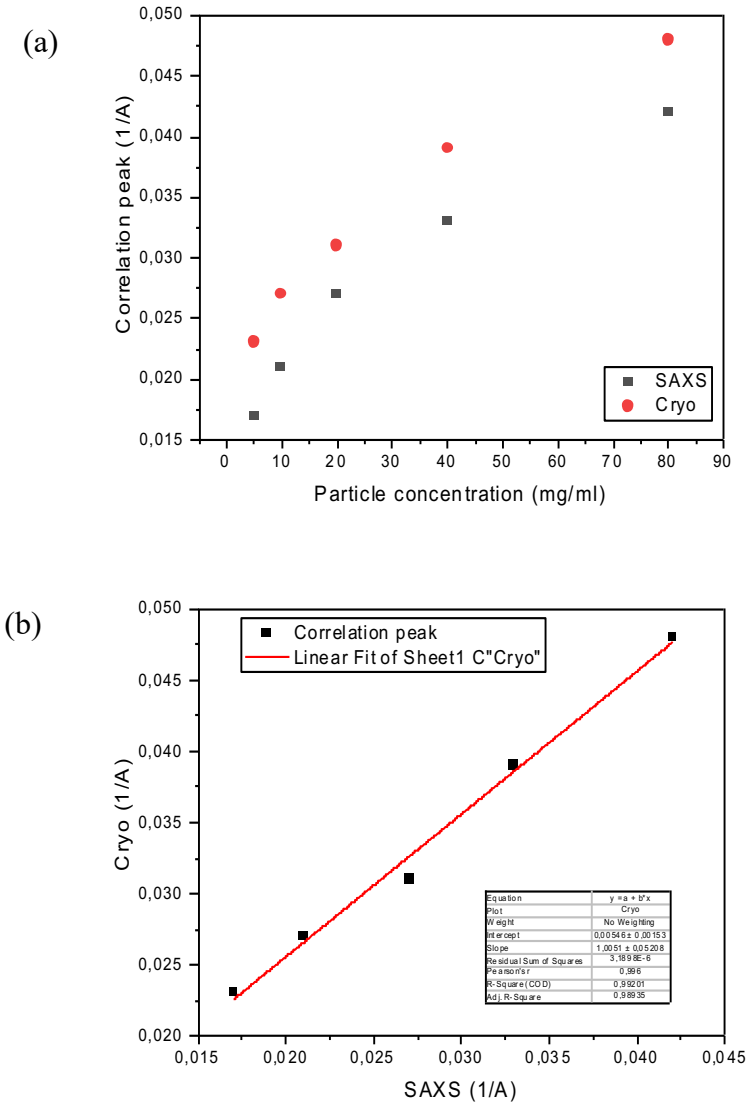

Figure 42: Linear regression analysis: (a) Correlation of the position peaks from Cryo-ET and SAXS for each concentration and (b) the linear fitting of the correlated peaks.

The value of the intercept with the y-axis is used for the subtraction and the shift of the structure factors curves experimentally obtained from Cryo-ET. The agreement between the two set of curves can be appreciated in Figure 43.

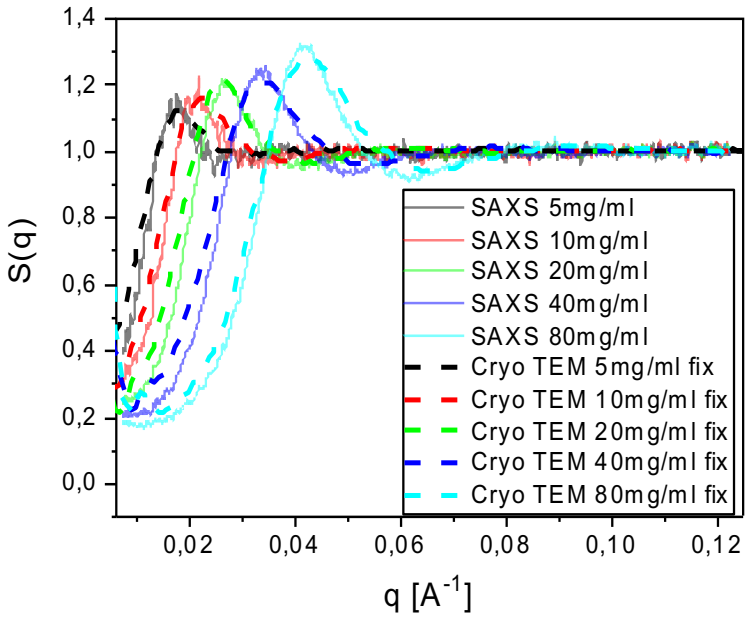

Figure 43: Structure factors S(q) of MUS-coated AuNPs in H_2O at different concentrations from Cryo-ET (dash lines) shifted in respect to the ones from SAXS (full lines).

In the case of the 30 mM NaCl nanoparticle dispersions at different concentrations, the structure factor profiles obtained from Cryo-ET match almost perfectly the ones derived by the scattering analysis especially at higher values of the scattering vector (Figure 44).
The curve for the 5 mg/mL nanoparticle concentration, for the same reason explained in the subsection 4.1.2.2, was almost flat and does not provide the structure factor and therefore it is not reported.

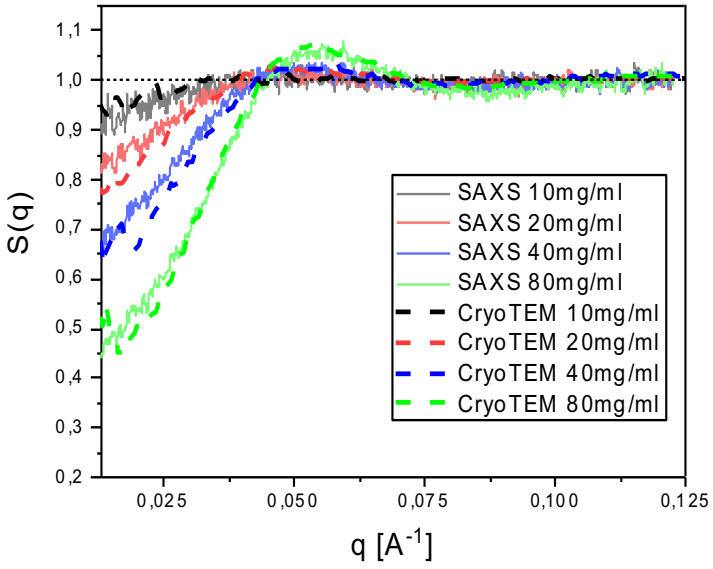

Figure 44: Structure factors S(q) of MUS-coated AuNPs in 30mM NaCl at different concentrations from Cryo-ET (dash line) and SAXS (full line) measurements.

From the SAXS profiles, the curves for the 5 mg/mL and the 10 mg/mL were overlapping. The scattering analysis confirms that the number density of the 5mg/mL solution is approximately the same as the 10 mg/mL in 30 mM NaCl. The low-quality data obtained with the concentrations of 5 and 10 mg/mL can be addressed to the low detection limit, the weakness of the blotting step in the sample preparation and the limited instrumentation. When sample thickness is higher and when using a microscope at higher voltages, for example, one can analyze a much larger sample and in this case the detection is more sensitive to the nanoparticle concentration and the count is higher.

As a conclusion, given the results and the matching obtained by the comparison of the structure factor from Cryo-ET and SAXS, it is possible to affirm that, considering the little shift due to concentration difference in the sample volume for the Cryo-ET,

$$S_{exp}\,(q)_{\,Cryo-ET} \equiv S_{exp}\,(q)_{\,SAXS}$$

and it is valid for media with different ionic strength. Therefore, these two techniques could be considered complementary and the devitrification process of the nanoparticles in the sample preparation does not modify and influence the state of the nanoparticle dispersions, it doesn't affect the interactions and it can be evaluated for different nanoparticles concentrations.

4.1.5 Discussion of Cryo-ET results using the DLVO Theory

The comparison between theoretical structure factors calculated using the DLVO theory with the ones experimentally derived from cryogenic electron tomography is evaluated. The DLVO model, as introduced in section 1.1, describes the pair interaction between two particles. It is defined for dilute colloidal dispersions and it doesn't consider the effects of the many-body system. The profiles obtained experimentally from cryogenic electron tomography are instead referred to the many-body interactions. Thus, a way to compare the two of them is required. There are different approaches to do this. The one which we focused on in this project relies on an analytical solution starting from the description of the system within DLVO theory as input parameters. The theoretical data are then manipulated using equations derived from statistical mechanics that allow the correlation with the experimental ones. The most important equation that explains the correlation between particles and provides the calculation of g(r) and S(q) from a determined pair interaction potential is the so-called Ornstein-Zernike (OZ) integral equation.

4.1.5.1 Ornstein-Zernike Integral Equation

The Ornstein-Zernike integral equation is used to correlate the pair interaction potential predicted by the DLVO theory with the experimental interaction potential for many-body interaction from Cryo-ET. This equation is called after the two scientists Leonard Salomon Ornstein and Frits Zernike that first presented it in 1914.
For the case of isotropic and homogeneous systems, this equation is expressed as

$$h(r_{12}) = c(r_{12}) + \rho \int c(r_{13})\, h(r_{23}) d\boldsymbol{r}_3 \qquad (8)$$

It relates the direct correlation function $c(r)$ with the total correlation function $h(r)$ for two particles 1 and 2 at a distance r_{12} with each other [42].
In particular, the total correlations among the particles $h(r)$ is defined as a sum of two contributions: a direct contribution (given by the direct correlation function $c(r)$) and an indirect contribution, which depends on the density of the system ρ and on the direct correlation for higher counts of neighbor particles [43].
The entire argument can be in fact iteratively solved with more intermediate particles, since the fluctuation at other distances affects the density, and it can be written as an infinite series equation

$$h(r_{12}) = c(r_{12}) + \rho \int c(r_{13})\, c(r_{23})\, d\boldsymbol{r}_3 + \rho^2 \int c(r_{13}) d\boldsymbol{r}_3 \int c(r_{24})\, c(r_{34}) d\boldsymbol{r}_4 + \ldots \quad (9)$$

The scheme for the derivation of this equation is illustrated in Figure 45.

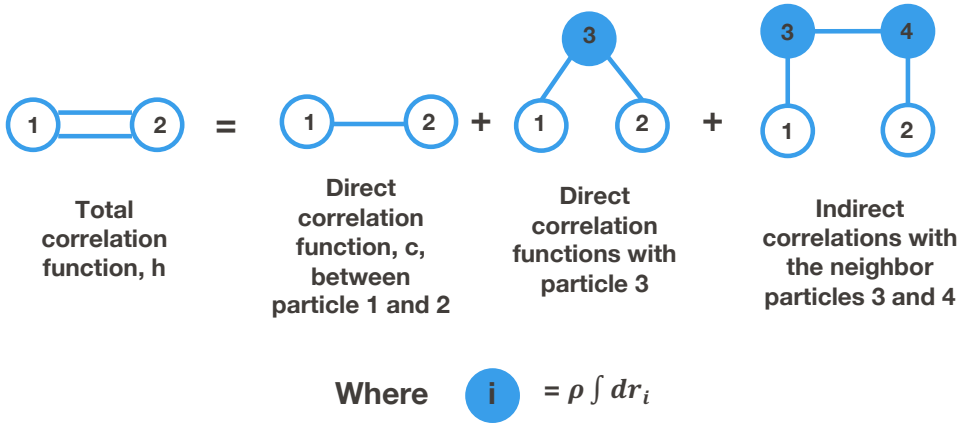

Figure 45: Total direct and indirect correlation functions between the particles in the system to derive the Ornstein-Zernike integral equation [40].

The total correlation function is also related to the radial distribution function:

$$h(r) = g(r) - 1 \quad (10)$$

The Ornstein-Zernike integral equation needs an additional closure relation in order to be solved, since there are two variables for just one equation. It is called closure relation because it closes the iterative loop and determines the solutions for the two variables. In this equation, the direct correlation function is expressed as a function of the pair potential u(r) and the total correlation function h(r).
The most common closure equations for the solution of the Ornstein Zernike integral equation are reported in Figure 46 [40].

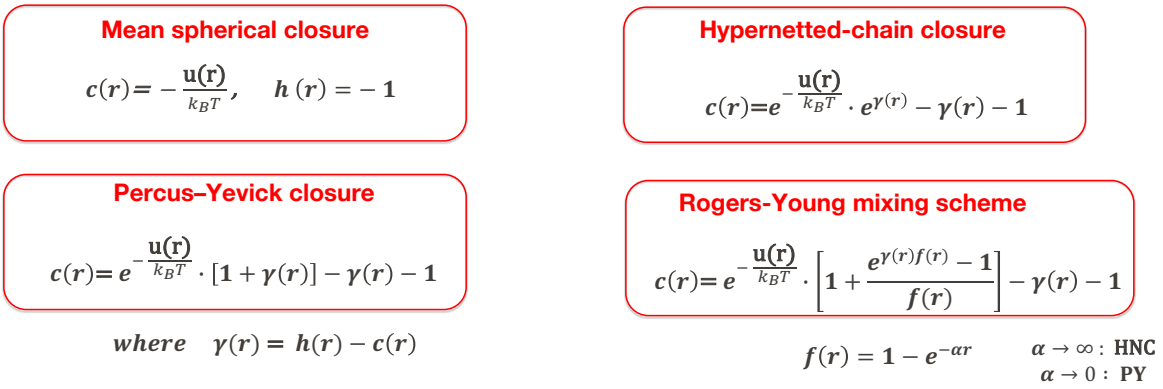

Figure 46: Most common addition closure relations for the solution of the Ornstein Zernike integral equation [40].

In the case of ionic fluids, the screening causes the exponential decrease of the total correlation function for large separation interparticle distance while the direct correlation decreases as a function of r^{-1} [43].
The Ornstein-Zernike equation can be generally written in terms of $r_{12} = r$, $r_{23} = r'$ and $r_{13} = |r - r'|$ as

$$h(r) = c(r) + \rho \int c(|\boldsymbol{r} - \boldsymbol{r}'|) h(r')\, d\boldsymbol{r}' \tag{11}$$

This equation can be studied in the reciprocal space and by using the so-called convolution theorem that states that the Fourier transform of the convolution of functions equals the product of the Fourier transform of these functions, thus easier to manipulate. The direct correlation function and the total correlation function can be written in the reciprocal space as $\hat{c}(q)$ and $\hat{h}(q)$ as the 3D Fourier transform of $c(r)$ and $h(r)$ respectively [37].
The OZ equation can then be written as

$$\hat{h}(q) = \hat{c}(q) + \rho \hat{c}(q) \hat{h}(q) \tag{12}$$

The structure facture can be expressed as a function of the direct correlation function:

$$S(q) = \frac{1}{1 - \rho \hat{c}(q)} \tag{13}$$

4.1.5.2 Calculation of the Structure factors from the DLVO theory

For the correlation analysis between the experimentally derived data and the theoretically calculated ones from the DLVO theory, the structure factors are considered for the study of the interactions for different concentrations of nanoparticles in the solution and for the presence of NaCl 30mM. As explained in section 3.2, the structure factor provides a measure of the local correlations related to the probability of finding a particle at a given distance from another.
The correlation method developed by Wu et al. (2014) is taken as a reference [33].
This method allows us to calculate the structure factors predicted by the theory and to fit them with the structure factors experimentally obtained from the cryogenic transmission electron microscopy tomography.

The first assumption is the modelling of the nanoparticles as charged hard spheres, that is for impenetrable spheres defined by σ as the hard sphere diameter, which interact via a hard-core Yukawa pair potential. In order to apply the DLVO theory for more complex systems, the component for the attractive interactions is usually replaced by the Yukawa pair potential that examines the interactions that are induced by the solvent [34].
The Yukawa pair potential can be expressed as

$$u(r) = \begin{cases} \infty & for\ r < \sigma \\ \dfrac{\sigma}{\pi\varepsilon_0\varepsilon_r}\left(\dfrac{Ze}{2+\kappa\sigma}\right)^2 \dfrac{e^{[-\kappa\sigma(r/\sigma-1)]}}{r/\sigma} & for\ r \geq \sigma \end{cases} \qquad (14)$$

where ε_0 and ε_r are the vacuum permittivity and the solvent relative permittivity, Ze is the charge carried by the nanoparticle, and κ is the Debye inverse length [44].
In the case of hard spheres, the radial distribution function is assumed equal to 0 for values of the separation distance inferior to the hard sphere diameter.
The theoretical S(q) is derived using the method for the solution of the Ornstein-Zernike integral equation proposed by Ginoza [45]. The closure relation chosen is the rescaled mean spherical approximation (RMSA), where the mean spherical approximation is improved by keeping the g(r) > 0 for small separation interparticle distances and is used when the strong repulsive long-range interactions cover the hard-core potential [43].
Thanks to the RMSA closure relation, the direct correlation function is comparable with the range of the interaction potential and describes c(r) for r > σ. In the rescaled MSA, the hard-core diameter is overestimated by introducing a parameter σ' is larger than σ. Hansen and Hayter (1982) proposed the presence of the *scaling parameter* s = σ / σ' < 1, where σ' is determined requesting the continuity of the radial distribution function: g (r ≡ σ') = 0, for the same number density [46].

The profiles calculated from the theory can be fitted by manipulating different parameters: the volume fraction, that depends on the number density of the nanoparticles, the charge per particle Ze and the scaling parameter s [41].
Once obtained the c(r) and then the h(r) we can derive the radial distribution function. From the RMSA-g(r) we can obtain the theoretical structure factors for the different nanoparticle concentrations by using the Fourier transform.
The scheme of the workflow for the comparison is illustrated in Figure 47.

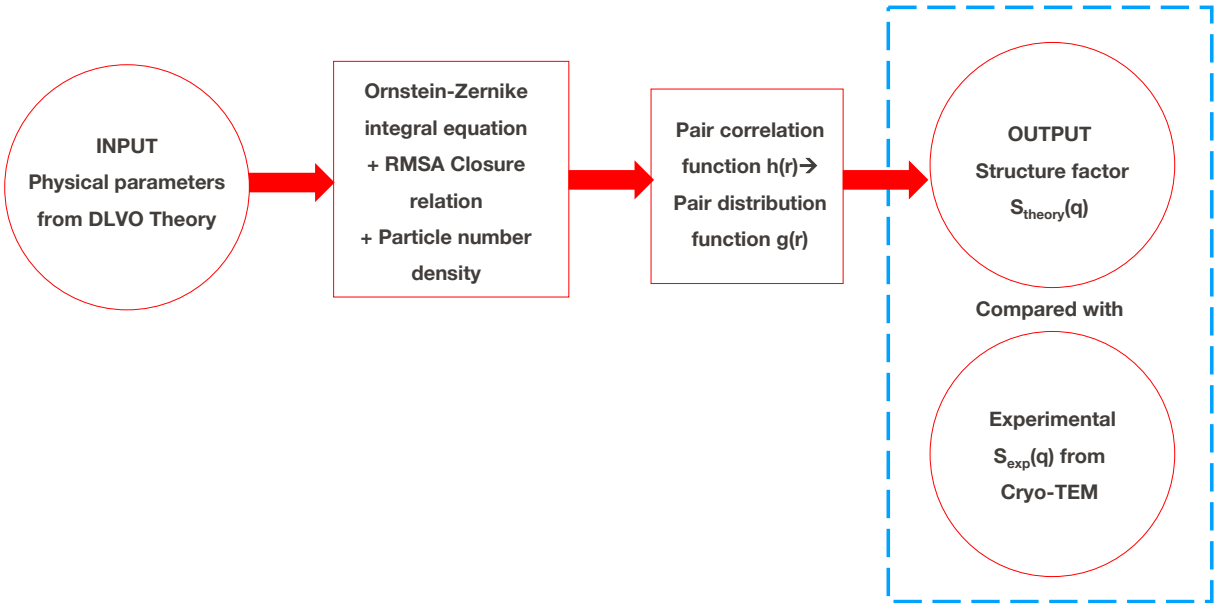

Figure 47: Workflow of the method used to correlate the data from the DLVO theory with the experimental data from cryogenic transmission electron microscopy tomography.

4.1.5.3 Comparison between theoretical and experimental structure factors for MUS-coated AuNPs in water

In Figure 48 are included the first set of RMSA- S(q) obtained with the analytical procedure for charged MUS-coated gold nanoparticles in Milli-Q water at temperature T = 298 K, with relative permittivity ε_r= 78,4 and the ionic strength I = 0.001 M at different concentrations (5, 10, 20, 40, 80 mg/mL), that interact via the Yukawa hard-core type DLVO pair potential.

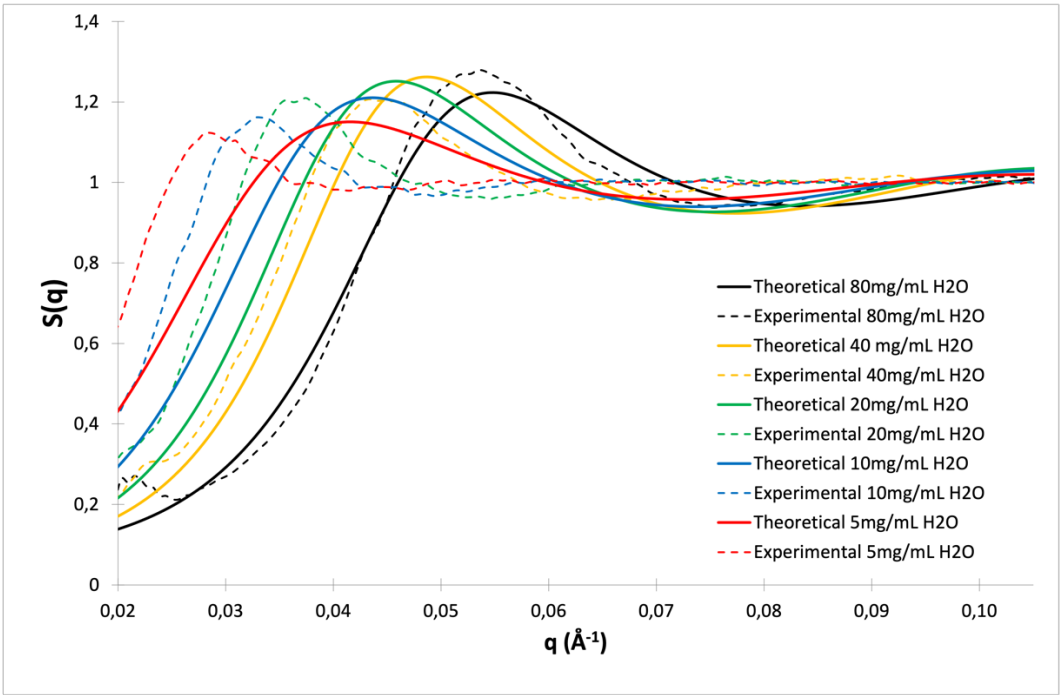

Figure 48: Theoretical structure factors S(q) (full line) of MUS-coated AuNPs in H_2O at different concentrations compared with the experimental ones obtained from Cryo-ET (dash lines).

As shown in the figure, the fitted curves derived by the DLVO theory model are not in agreement with the experimental structure factors from Cryo-ET for the different concentrations of the nanoparticles. The value of the scaling parameter is select to be equal to 0.3 for all the different concentration in order to overestimate the diameter with the presence of the ligand (σ'= 5 nm, which approximately corresponds to the nanoparticle total diameter). The features of the curves appear clear but the fitting between the theoretical and experimental data is not very remarkable, especially for low concentrations where the theory fails to describe the long-range interactions. The problem with the fitting can be related to different reasons. One of these can be related to the fact that, when the nanoparticles are in a solution, the conformations of the ligands are dependent on their interactions with the solvent and it can perturbate their distribution as a function of the nanoparticle concentration. The complexity of these conformations can cause further deviations from the theory [47]. The next approach is to select a parameter that can be modified in order to improve the fitting and better predict the experimental data. For this analysis, a single fit starting from one concentration is performed and later applied to the other concentrations. The variation of the scaling parameter is used as the fitting parameter for each concentration.
The new curves obtained by fitting the data by changing the scaling parameter are reported in Figure 49.

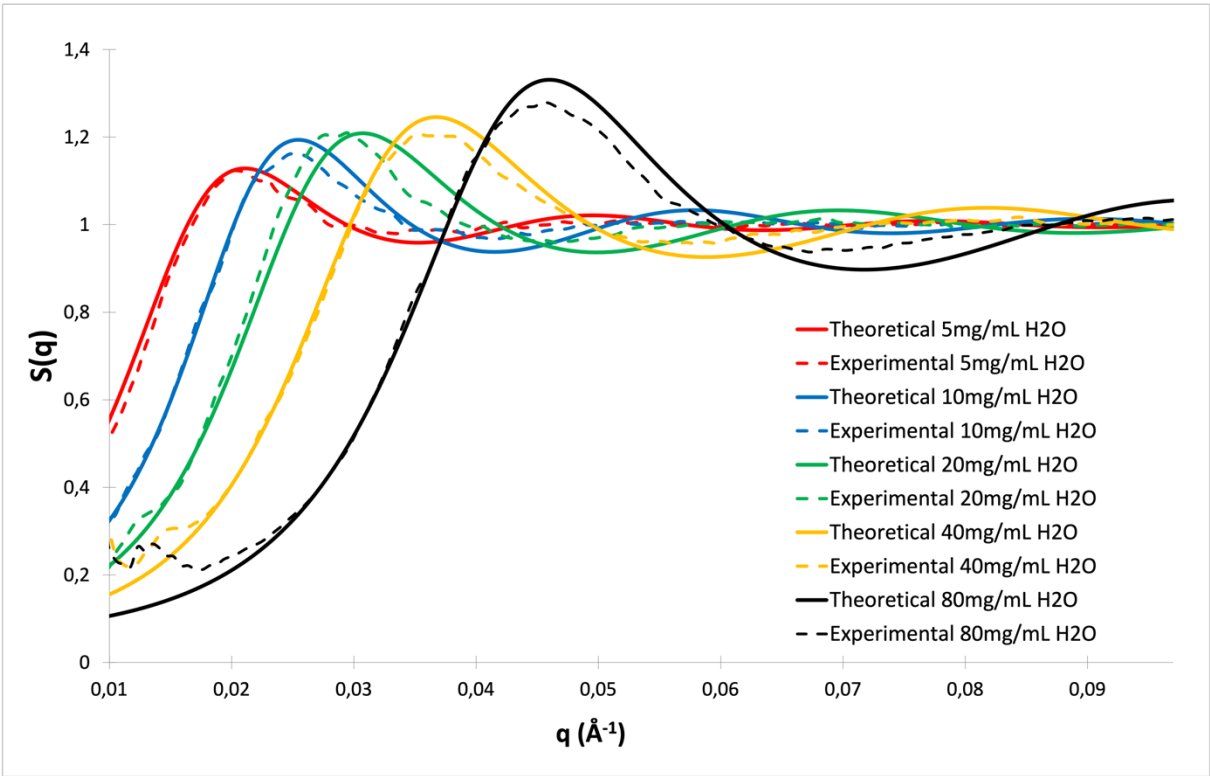

Figure 49: Improved fitting for the theoretical structure factors S(q) (full line) of MUS-coated AuNPs in H_2O at different concentrations compared with the experimental ones obtained from Cryo-ET (dash lines).

For this calculation, the physical parameters remained the same, while the parameter modified for the improvement of the fitting is the scaling parameter s.
The values used for the fitting of the scaling parameter are reported in Table 2.

Concentration	Fitted scaling parameter s
5 mg/mL	0.13
10 mg/mL	0.15
20 mg/mL	0.18
40 mg/mL	0.21
80 mg/mL	0.25

Table 2: Scaling parameter for the fitting of the theoretical structure factors for the different concentrations

The best-fit profiles of the theoretical structure factors after this implementation agree well in the low range of the scattering vector q, but still do not agree very well for higher values of the scattering vector. In particular, the values of the scaling parameter chosen for the improved fitting increase with increasing the concentration. The new diameter σ' decreases and that can be explained by the different conformations of the ligands for different concentrations, where they arrange in a different way for higher concentrations of nanoparticles in the solution.

In conclusion, it can be stated that the theory gets some part of the physics, such as the concentration dependence, the repulsions, but is not able to describe and correlate the overall stability of the nanoparticle dispersions.

4.1.5.4 Comparison between theoretical and experimental structure factors for MUS-coated AuNPs in 30mM NaCl

The RMSA- S(q) for charged MUS-coated gold nanoparticles in a 30mM sodium chloride dispersions is obtained with the same method as before at temperature T = 298 K, with relative permittivity ε_r= 62,8 and ionic strength I = 0.03 M, for different concentrations (5, 10, 20, 40, 80 mg/mL), that interact via the Yukawa hard-core type DLVO pair potential, and is reported in Figure 50.

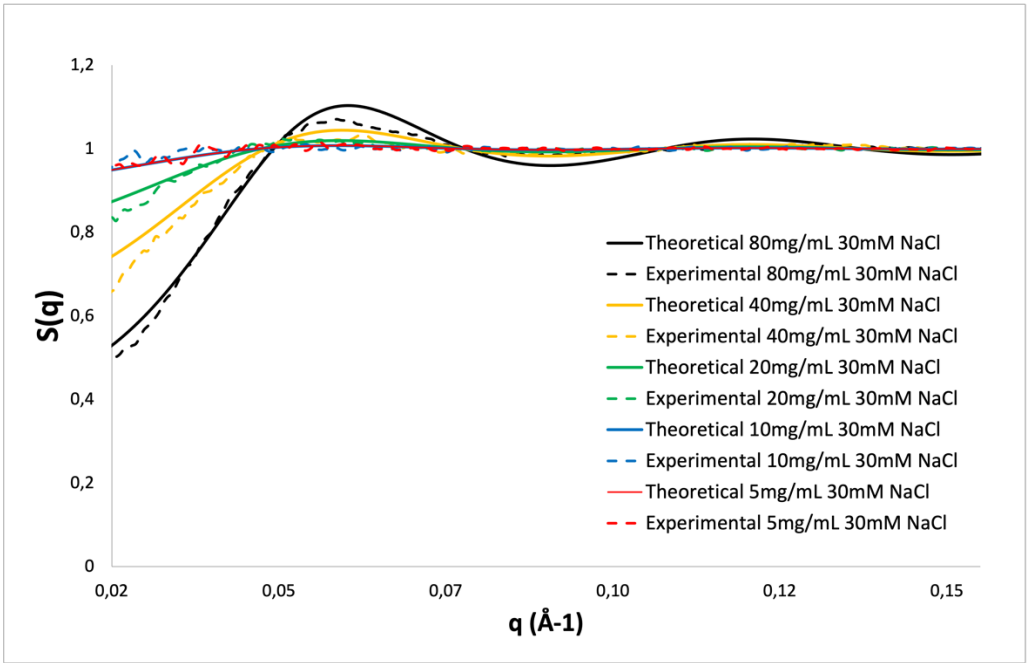

Figure 50: Theoretical structure factors S(q) (full line) of MUS-coated AuNPs in NaCl 30mM at different concentrations compared with the experimental ones obtained from Cryo-ET (dash lines).

In the case of the presence of salt, with fixed scaling parameter s = 0.3, the overall correlation seems to be more evident than the case of water solution. The fitting of the theoretical structure factors with the ones from cryogenic electron tomography is clear but still can be improved. To do this, new values of the scaling parameter are found to better fit the data calculated from the theory. The improved curves are shown in Figure 51.

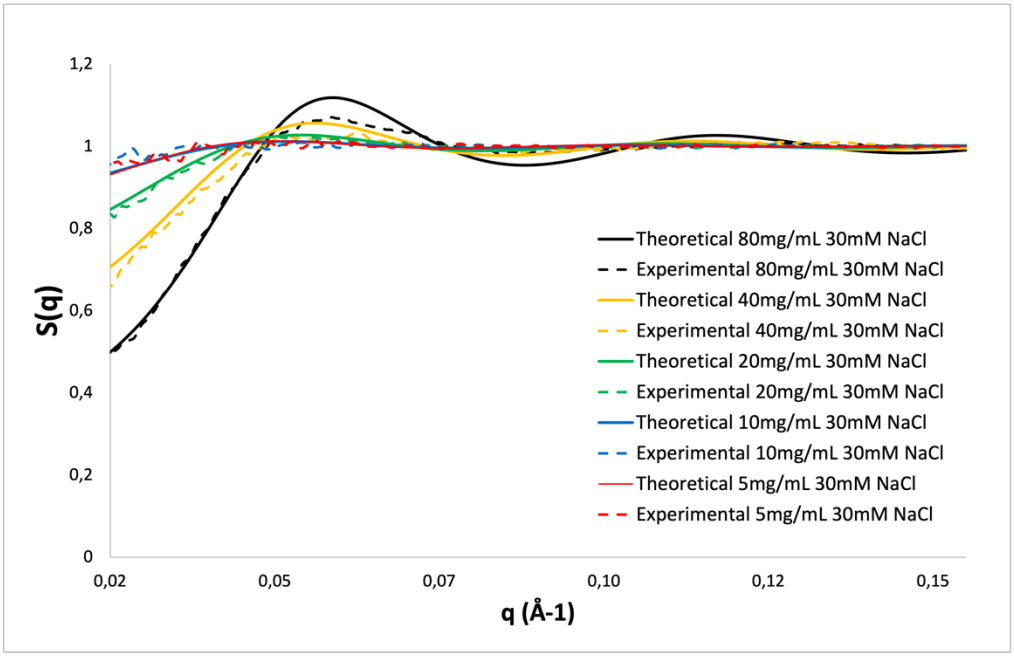

Figure 51: Improved fitting of the theoretical structure factors S(q) (full line) of MUS-coated AuNPs in NaCl 30mM at different concentrations compared with the experimental ones obtained from Cryo-ET (dash lines).

The values used for the fitting of the scaling parameter are reported in Table 3.

Concentration	Fitted scaling parameter s
5 mg/mL	0.25
10 mg/mL	0.26
20 mg/mL	0.27
40 mg/mL	0.28
80 mg/mL	0.29

Table 3: Scaling parameter for the fitting of the theoretical structure factors for the different concentrations

The curves of the profiles for the 10 mg/mL and 5 mg/mL are characterized by having a very weak interaction, they are flat and the features are less pronounced. Because of this, the curves in this case don't allow the confirmation of a good fitting. The analysis is then focused on the comparison for the cases of higher concentration such as the 80, 40 and 20 mg/mL curves.
The more evident match for nanoparticles in the solution with NaCl 30 mM can be related to the fact that the electrostatic interaction is screened. From the theory, in case of big particles, the electrostatic contribution is still compensated by the van der Waals interaction. Instead, in case of small particles, with high density of charge, they can be assumed acting as macroions and so the description is focused around the interactions between them and therefore it deviates from the experimental conditions.

4.2 Effect of Temperature on PNIPAM-coated gold nanoparticles interactions

4.2.1 Analysis of the temperature sensitivity of the PNIPAM-coated Gold Nanoparticles

For the second part of the project, a couple of tests are conducted in order to evaluate and observe the thermo-responsive behavior of the PNIPAM-coated gold nanoparticles prepared. To determine and verify their behavior at higher temperatures, 1 mg/mL of nanoparticle dispersions for PNIPAM 3 kDa and 6 kDa are prepared in glass vials and immersed from an ice bath to a hot bath (around 40°C). Despite trying different heating sources such as oven, heating gun, hot plate on the magnetic stirrer at even higher temperatures (the highest value reached was around 80°C for 4 hours), in all of these cases still no temperature responsive behavior could be observed, as there are no signs of color change and nanoparticles aggregation. Recent studies reported about the unobvious temperature sensitivity of PNIPAM-coated gold nanoparticles. Jones et al. (2016) claimed that the aggregation of the PNIPAM-coated gold nanoparticles is strongly influenced by impurities from the unbound PNIPAM in the solution, rather than the PNIPAM that is anchored on the nanoparticles themselves. In particular, the aggregation depends on the concentration of the free polymer and on the fact that its presence increases the solution turbidity, a characteristic that proves the nanoparticles aggregation. In addition, complete aggregation occurs only above a critical concentration of this free PNIPAM [48].

In case of clean and purified dispersions of nanoparticles, heating above the LCST does not cause change in solution color, as the PNIPAM chains collapse but they do not cause nanoparticle's aggregation. Thus, the conclusion is that the thermo-responsive behavior is visible only in impure systems, but not visible in nanoparticle dispersions without any impurities. This is also the indirect proof that we had effectively purified and obtained clean nanoparticles.

The induction of aggregation in a purified PNIPAM-coated gold nanoparticles solution has been demonstrated by the addition of salt in the solution. This lowers the LCST and causes the aggregation of the nanoparticles at lower temperatures. The actual contribution of salt in the nanoparticles' aggregation consists in the screening of the charges on the surface nanoparticles, so the electrostatic repulsion between the PNIPAM-coated gold nanoparticles decreases. Thanks to the "*salting out effect*", i.e. the dehydration of the PNIPAM that is caused by the addition of the salt, the hydrophobic interaction between the nanoparticles increases and the nanoparticles can agglomerate above the lower critical solution temperature [49].

Li et al. (2021) [50] recently proposed a mechanism that shows two different scenarios. In the first one, without the presence of the sodium chloride, the conformational change due to the increase of temperature above the LCST is restrained by the hydrogen bonds that are generated among PNIPAM ligands, therefore no aggregation behavior or change in turbidity occurs. However, in the second case, when salt is added in the system, the reduction of the double layer decreases the electrostatic repulsion due to the NaCl screening, enhancing the aggregation, which is mainly induced by the electrostatic repulsion rather than being caused by the conformational change of the PNIPAM itself. Above the critical temperature, the negative charge increases due to the adsorption of the chloride ions which destabilizes the hydrogen bonding between the amide and water through polarization. This enhances the dehydration of PNIPAM chains and provides aggregation. Moreover, for high NaCl concentration, the increasing negative charges of the PNIPAM gold nanoparticles due to the bond between Cl^{-1}

and NH groups determine a strong interaction between the PNIPAM ligands attached to the gold nanoparticles. This mechanism is presented in Figure 52 [50].

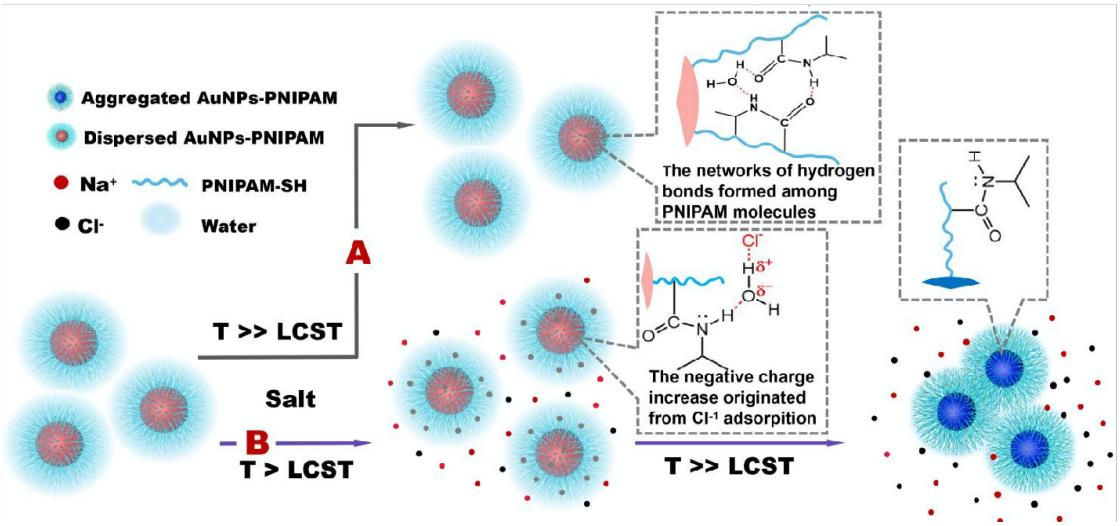

Figure 52: Thermosensitive behavior of PNIPAM AuNPs in different conditions: (A) the effects of the increase of temperature above the LCST and (B) the addition of salt [50].

To test the thermo-responsive behavior after the addition of salt, the PNIPAM-coated gold nanoparticles are dissolved in 150 mM of NaCl, and then heated up at 80°C on the magnetic stirrer. The aggregation is observed after 40 minutes (Figure 53).

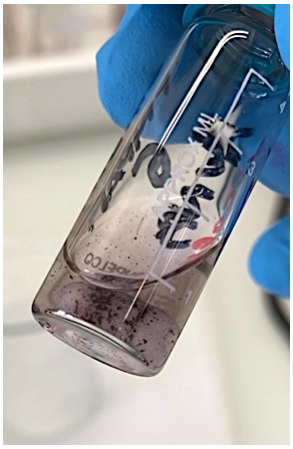

Figure 53: PNIPAM Gold Nanoparticles aggregates that are visible on the magnetic bar.

The vial is then immersed once again in the ice bath, and already after a few seconds the nanoparticles are dissolved again and the solution returned to its original color, confirming the reversibility of the system.

4.2.2 Cryo-TEM Analysis

Last step of the project is the characterization of the behavior of the PNIPAM-coated gold nanoparticles using cryogenic transmission electron microscopy (Cryo-TEM) while trying to evaluate their behavior at different temperatures. The first set of samples is prepared at room temperature (23°C) with a relative humidity of 100%. This represents the control sample to which the future results will be compared. In this case the nanoparticles appeared very well dispersed and distributed in the amorphous ice layer, where no aggregates are present.
For the characterization of the sample at higher temperature, the preparation proved to be more complex and crucial. Two different kinds of Cryo-TEM grids are used: Lacey Carbon film, 200 mesh copper grid and Holey Carbon film, 200 mesh copper grid.
The Holey film has less holes and therefore more carbon film as substrate, while the first one has a bigger percentage of open area. We used both of them to evaluate if the presence of the substrate influences the nanoparticles distribution on the grids.
To test the thermo-responsive behavior of the PNIPAM gold nanoparticles, during sample preparation the climate chamber of the Vitrobot Mark IV is set at 50°C (the highest temperature reachable of this instrument is around 60°C). Whilst operating at these high temperatures, it is very difficult to maintain the relative humidity of the chamber at high values; in this case, the max value reached was around 70-75%.
Grids covered with 5 μL of the nanoparticle dispersion are prepared and kept in the chamber at these conditions, blotted and then immersed in liquid ethane and preserved in liquid nitrogen.
Analysis of prepared samples showed that most of them are almost completely broken, there are only small holes isolated that are intact. No full stable layer that can be considered reproducible is obtained. The main reason for this is most probably based on the fact that at these high temperatures the carbon film is unstable and it easily breaks. For both the Lacey and the Holey Carbon films, the bigger holes are empty and the hole spacing is destroyed. Only a few small holes are filled and intact. Despite the overall condition of the grid, these few intact holes are in fact showing the predicted thermo-responsive behavior and the formation of aggregates. The results can be appreciated in Figure 54. Nonetheless, better systems should be found in the future to fully evaluate observed effects.

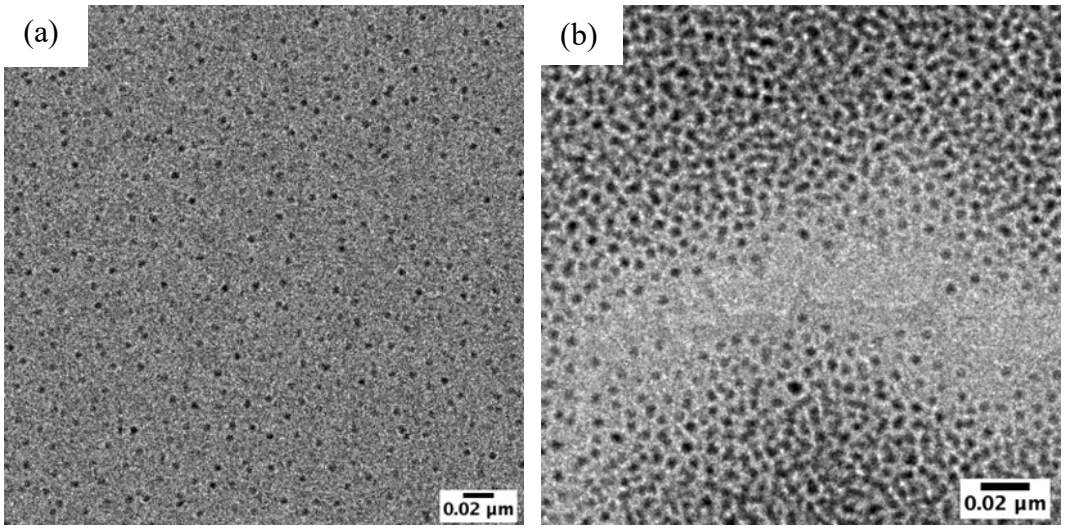

Figure 54: (a) Cryo-TEM images of PNIPAM 6kDa AuNPs at room temperature and 100% relative humidity and (b) at 50°C and 73% relative humidity.

Next step is focused on the analysis of the PNIPAM-coated gold nanoparticles behavior at slightly elevated temperature of 35 °C (to avoid destruction of the grids but still above the LCST of pure PNIPAM) and with the additional presence of the NaCl to induce aggregation of nanoparticles, as described in the previous sub-section. For this purpose, a solution of 10mg/mL PNIPAM AuNPs in 100mM of NaCl is prepared. Both kinds of grids appear stable and at higher temperature aggregated nanoparticles can be seen (Figure 54b). Infact, also in this case, at temperatures higher than the phase transition point, Cryo-TEM shows globular aggregate states in presence of isolated nanoparticles, suggesting a micellar-like reversible aggregation mechanism. The relative humidity during the preparation of this grid is still pretty low, around 77%. Therefore, the reason for the grids' breakage during the sample preparation is mainly due to the high temperature and not the low relative humidity. To confirm that the aggregation of the nanoparticles is caused only by a combination of both salt and increased temperature, Cryo-TEM images of the same system (10 mg/mL PNIPAM AuNPs in 100 mM of NaCl) at room temperature (23°C) and 100% of relative humidity are acquired (Figure 55). As presented, the nanoparticles are evenly dispersed, and it is possible to conclude that the temperature is the effective driving force of nanoparticles aggregation and the presence of salt is able to lower the temperature at which the volume phase transition takes place.

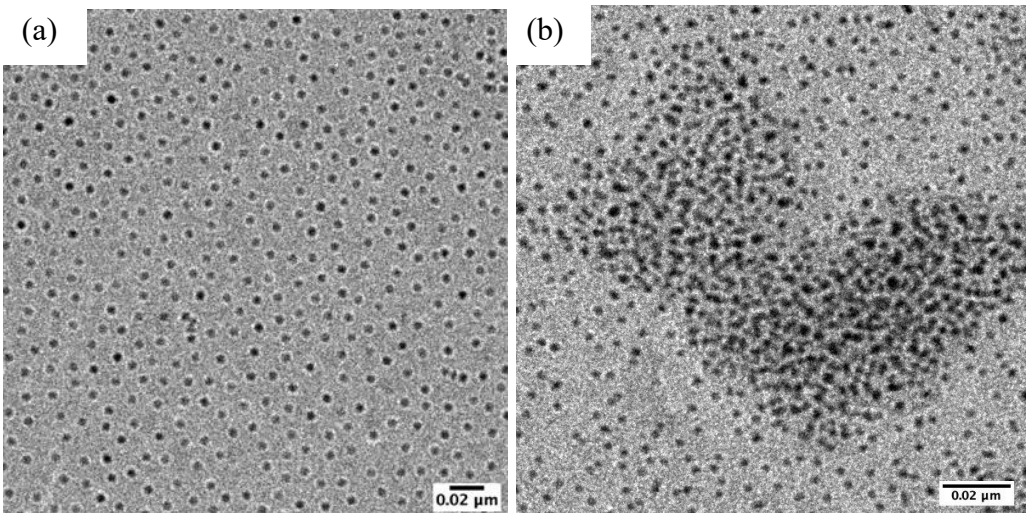

Figure 55: (a) Cryo-TEM images of PNIPAM 6kDa AuNPs in 100 mM NaCl at room temperature and 100% relative humidity and (b) at 35°C and 77% relative humidity.

5. Conclusions and future work

The quantitative study of the interactions between MUS-coated gold nanoparticles as a function of their concentration, the presence of salt in the dispersions and the qualitative analysis of the effect of temperature on PNIPAM-coated gold nanoparticles are conducted.
The relation between the two main techniques used in this project to characterize the nanoparticles is defined and assessed. In particular, the structure factors S(q) from both cryogenic transmission electron microscopy tomography and small angle X-ray scattering are compared in the cases of ultrapure water and 30mM NaCl dispersions for different nanoparticle concentrations.
The comparison between theoretical structure factors calculated using the DLVO theory with the one experimentally derived from Cryo-ET is evaluated.
The structure factors allow to quantitatively compare and correlate the interactions between the nanoparticles in the dispersions between the experimentally derived data and the theoretically calculated ones from the DLVO theory, the structure factors are considered for the study of the interactions for different concentrations of nanoparticles in the ultrapure water and the case of 30mM NaCl dispersions.
The theoretical S(q) are derived using a method based on the rescaled mean spherical approximation solution proposed by Ginoza of the Ornstein-Zernike integral equation, with the assumption of a hard spheres model and Yukawa pair potential [45]. The fitting of the curves calculated from the theory with the experimental curves can be improved by manipulating the scaling parameter s that shows a better fitting with the experimentally derived data, especially at low values of the scattering vector q. In order to prove different comparisons with the theory and test different solutions, other methods can be used in the future. Future studies and challenges may also quantify the interactions between gold nanoparticles coated with 11-mercapto-1-undecane sulfonate together with 1-octanethiol, MUS:OT, with both a charged ligand (MUS) and an hydrophobic ligand (OT), where the interaction is stronger.
PNIPAM-coated gold nanoparticles proved to be a good reference model to study the aggregation behavior among the nanoparticles as a function of the increase of the temperature and the presence of salt. The PNIPAM-coated gold nanoparticles can be further addressed in the future through the quantitative estimation of the interactions between nanoparticles at different temperatures and media with different ionic strength, and the study of the critical micelle concentration for these systems. Their aggregation behavior can be also estimated with the help of cryogenic transmission electron tomography.

6. List of Figures

References

[1] Barreto Â., Luis L.G., Girão A. et al., Behavior of colloidal gold nanoparticles in different ionic strength media, 2015, *J Nanopart Res* 17, 493, [doi:10.1007/s11051-015-3302-0]

[2] Larguinho M., Baptista P.V., Gold and silver nanoparticles for clinical diagnostics—from genomics to proteomics, 2012, *J Proteomics* 75:2811–2823

[3] Pamies R., Cifre J.G.H., Espín V.F. et al., Aggregation behaviour of gold nanoparticles in saline aqueous media, 2014, J Nanopart Res 16, 2376, [doi:10.1007/s11051-014-2376-4]

[4] Wijenayaka L. A., Michael R. Ivanov M. R., Cheatum C. M. et al., Improved Parametrization for Extended Derjaguin, Landau, Verwey, and Overbeek Predictions of Functionalized Gold Nanosphere Stability, 2015, *J. Phys. Chem. C*, 119, 10064−10075, [doi: 10.1021/acs.jpcc.5b00483]

[5] Hotze E.M., Phenrat T., Lowry G.V., Nanoparticle aggregation: challenges to understanding transport and reactivity in the environment, 2010, *J Environ Qual*.; 39(6):1909-24, [doi: 10.2134/jeq2009.0462]

[6] Gregor Trefalt and Michal Borkovec, Overview of DLVO Theory, 2014, www.colloid.ch/dlvo

[7] Gatica, S., Cole M., and Velegol D., Designing van der Waals forces between nanocolloids, 2005, *Nano Lett*. 5:169–173

[8] Heuer-Jungemann A., Feliu N., Bakaimi I. et al., The Role of Ligands in the Chemical Synthesis and Applications of Inorganic Nanoparticles, 2019, *Chemical Reviews*, 119 (8), 4819-4880. [doi: 10.1021/acs.chemrev.8b00733]

[9] https://pubchem.ncbi.nlm.nih.gov/compound/11-Mercaptoundecane-1-sulfonate

[10] Häkkinen H., The Gold–Sulfur Interface at the Nanoscale, 2012, *Nat. Chem*., 4, 443. [doi: 10.1038/nchem.1352]

[11] Gasbarri, M., Stellacci, F., Tapparel, C., Cagno V. et al., SARS-CoV-2 Inhibition by Sulfonated Compounds, 2020, *Microorganisms,* 8(12), 1894. [https://doi.org/10.3390/microorganisms8121894]

[12] Yang Y., Serrano L. A., Guldin S., A Versatile AuNP Synthetic Platform for Decoupled Control of Size and Surface Composition, 2018, *Langmuir*, 34 (23), 6820-6826, [doi: 10.1021/acs.langmuir.8b00353]

[13] Peng S., Lee Y., Chao Wang C., A Facile Synthesis of Monodisperse Au Nanoparticles and Their Catalysis of CO Oxidation, 2008, *Nano Res.*, 1: 229 234, [doi: 10.1007/s12274-008-8026-3]

[14] https://pubchem.ncbi.nlm.nih.gov/compound/Oleylamine

[15] De la Presa P., Multigner M., De la Venta J. et al., Structural and magnetic characterization of oleic acid and oleylamine-capped gold nanoparticles, 2006, *Journal of Applied Physics,* 100, 123915, [doi: 10.1063/1.2401314]

[16] Guo C., Yarger J.L., Characterizing gold nanoparticles by NMR spectroscopy, 2018, *Magn Reson Chem*.; 56:1074–1082 [doi: 10.1002/mrc.4753]

[17] Su W., Yang M., Zhao K. et al., Influence of Charged Groups on the Structure of Microgel and Volume Phase Transition by Dielectric Analysis, 2016, *Macromolecules*, 49, 7997−8008 [doi:10.1021/acs.macromol.6b00809]

[18] Kawaguchi H., On Going to a New Era of Microgel Exhibiting Volume Phase Transition, 2020, *Gels*, 6(3), 26; [doi: 10.3390/gels6030026]

[19] Li C., Wang C., Ji Z., et al., Synthesis of thiol-terminated thermoresponsive polymers and their enhancement effect on optical limiting property of gold nanoparticles, 2019, European Polymer Journal 113, 404–410 [doi: 10.1016/j.eurpolymj.2019.02.009]

[20] Bhella D., Cryo-electron microscopy: an introduction to the technique, and considerations when working to establish a national facility, 2019, *Biophys Rev.,* 11(4): 515–519, [doi: 10.1007/s12551-019-00571-w]

[21] Cryo-Electron Microscopy, What it is, How it Works, Pros and Cons, Microscope Master, https://www.microscopemaster.com/cryo-electron-microscopy.html

[22] Kuntsche J., Horst J. C., Bunjes H., Cryogenic transmission electron microscopy (cryo-TEM) for studying the morphology of colloidal drug delivery systems, 2011, *International Journal of Pharmaceutics*, Volume 417, Issues 1–2, Pages 120-137, [doi.org/10.1016/j.ijpharm.2011.02.001]

[23] MyScope training, Microscopy Australia, https://myscope.training/#/TEMlevel_3_3

[24] Ted Pella Inc., Microscopy products for Science and Industries, https://www.tedpella.com/easiGlow_html/Glow-Discharge-Cleaning-System.htm

[25] Vitrobot Protocol, Johns Hopkins School of Medicine, https://cryoem.jhmi.edu/protocols/vitrobot-protocol/

[26] Murata K., Wolf M., Cryo-electron microscopy for structural analysis of dynamic biological macromolecules, 2018, *Biochimica et Biophysica Acta (BBA) - General Subjects*, Volume 1862, Issue 2, Pages 324-334, [doi.org/10.1016/j.bbagen.2017.07.020]

[27] Focus on: Cryo-electron microscopy, The Biologist, Royal Society of Biology, https://www.rsb.org.uk/biologist-features/focus-on-cryo-electron-microscopy

[28] Liu L., Boldon L., Urquhart M., Wang X., Small and Wide Angle X-Ray Scattering Studies of Biological Macromolecules in Solution, 2013, *J. Vis. Exp*. (71), e4160, [doi:10.3791/4160]

[29] Kikhney A. G., Svergun D. I., A practical guide to small angle X-ray scattering (SAXS) of flexible and intrinsically disordered proteins, 2015, *FEBS Letters* 589 2570–2577, [http://dx.doi.org/10.1016/j.febslet.2015.08.027]

[30] Mertens H., Svergun D. I., Combining NMR and small angle X-ray scattering for the study of biomolecular structure and dynamics, 2017, *Archives of Biochemistry and Biophysics*, Volume 628, Pages 33-41, [https://doi.org/10.1016/j.abb.2017.05.005]

[31] Sanjeeva Murthy N., Recent Developments in Small-Angle X-Ray Scattering, 2017, Spectroscopy, Special Issues, Volume 32, Issue 11, Pages: 18–24

[32] Craievich A., Institute of Physics, University of São Paulo Advanced School on Synchrotron and Free Electron Laser Sources and their Multidisciplinary Applications Conference, 2008, Trieste, Italy

[33] Wu C., Chan D. Y. C., Tabor R. F., A simple and accurate method for calculation of the structure factor of interacting charged spheres, 2014, *J Colloid Interface Sci*; 426:80-2. [doi: 10.1016/j.jcis.2014.03.023]

[34] Morita T., Uehara N., Kuwahata K. et al., Interaction Potential between Biological Sensing Nanoparticles Determined by Combining Small-Angle X-ray Scattering and Model Potential-Free Liquid Theory, 2016, *J. Phys. Chem. C*, 120, 25564−25571, [doi: 10.1021/acs.jpcc.6b06487]

[35] Grishaev A., Sample preparation, data collection, and preliminary data analysis in biomolecular solution X-ray scattering, 2012, *Curr Protoc Protein Sci.;* Chapter 17: Unit17.14. [doi:10.1002/0471140864.ps1714s70]

[36] Kopera B. A. F., Retsch M., Computing the 3D Radial Distribution Function from Particle Positions: An Advanced Analytic Approach, 2018, *Analytical Chemistry*, 90 (23), 13909-13914, [doi: 10.1021/acs.analchem.8b03157]

[37] Hammouda B., Probing Nanoscale Structures – The Sans Toolbox Structure factors for particulate systems, Chapter 32

[38] Lynch M. L., Kodger T., Weaver M. R., Anticipating colloidal instabilities in cationic vesicle dispersions by measuring collective motions with dynamic light scattering, 2006, *Journal of Colloid and Interface Science*, Volume 296, Issue 2, Pages 599-607, [https://doi.org/10.1016/j.jcis.2005.09.048]

[39] Cortada M., Anta J.A., Molina-Bolívar J. A., Secondary minimum coagulation in charged colloidal suspensions from statistical mechanics methods, 2007, *J Phys Chem B.*; 111(5):1110-8. [doi: 10.1021/jp0661589. PMID: 17266264]

[40] Nägele G., Dynamics of Dispersion colloids, 2005, Lecture Notes, Institute of SolidState Physics (IFF) Soft Matter Division

[41] Vérétout F., Delaye M., Tardeieu A., Osmotic pressure and X-ray analysis of alfa-cristallin solutions, 1989, *J. Mol. Biol*. 205, 713-728

[42] Case D., Manby F., The Ornstein-Zernike equation in molecular electronic structure theory, 2010, *Molecular Physics*, Taylor & Francis, 108 (03-04), pp.307-314. 10.1080 / 00268970903446772. hal-00580688

[43] Nägele G., The Physics of Colloidal Soft Matter, 2004, Lecture Notes, Centre of excellence for advanced materials and structures

[44] Maarouf A., Elhasnaoui K., Badia M. et al., Numerical Study of the Structure and Thermodynamics of Colloidal Suspensions by Variational Method, 2014, *Sop Transactions On Applied* Physics [doi: 10.15764/Aphy.2014.04002]

[45] Ginoza M., Mean spherical approximation solution of Ornstein-Zernike Equation in a charged hard sphere system with screened coulombic interactions, 1985, *Journal of the Physical Society of Japan*, Vol. 54. No. 8, pp. 2783-2785

[46] Hansen JP., Hayter J. B., A rescaled MSA structure factor for dilute charged colloidal dispersions, *Molecular Physics,* 1982, 46:3, 651-656, [doi: 10.1080/00268978200101471]

[47] Liepold C., Smith A., Lin B. et al., Pair and many-body interactions between ligated Au nanoparticles, 2019*, J. Chem. Phys*. 150, 044904; [https://doi.org/10.1063/1.5064545]

[48] Jones S.T., Walsh-Korb Z., Barrow S.J. et al., The Importance of Excess Poly(N-isopropylacrylamide) for the Aggregation of Poly(N-isopropylacrylamide)-Coated Gold Nanoparticles, 2016, *ACS Nano*, 10, 3158−3165, [doi: 10.1021/acsnano.5b04083]

[49] Zhang Z., Maji S., Da Fonseca Antunes A. et al., Salt Plays a Pivotal Role in the Temperature-Responsive Aggregation and Layer-by-Layer Assembly of Polymer-Decorated Gold Nanoparticles, 2013*, Chem. Mater*., 25, 4297−4303, [doi: 10.1021/cm402414u]

[50] Li R., Cheng C., Wang Z., et al., 2021, Conformational Stability of Poly (N-Isopropylacrylamide) Anchored on the Surface of Gold Nanoparticles, *Materials*; 14(2):443. [doi: 10.3390/ma14020443]

Acknowledgements

Desidero vivamente ringraziare i Professori Marco Sangermano e Francesco Stellacci per avermi permesso di svolgere la tesi magistrale presso l'EPFL e per aver creduto in me nell'affidarmi questo progetto.
Vorrei ringraziare il Dr. Quy Ong per avermi seguito passo passo e avermi aiutata durante lo svolgimento di questo lavoro.
Un grazie molto sentito anche a Dr. Lukasz Richter con cui ho collaborato nella parte di sintesi e caratterizzazione delle nanoparticelle per essere stato un punto di riferimento in questi mesi.
Grazie a Dr. Davide Demurtas il quale è sempre stato disponibile ad aiutarmi nei momenti di difficoltà durante l'utilizzo del microscopio crioelettronico.
Grazie a Camilla, Ting e tutti gli altri colleghi del SuNMIL per le belle giornate trascorse insieme.
Un grazie di cuore alla mia famiglia che mi ha sempre sostenuto e a tutti i miei amici e colleghi del Politecnico di Torino per le risate e il supporto nei momenti difficili.